 doi:10.20944/preprints202106.0462.v1

Article

A novel approach to global positioning system accuracy assessment, verified on LiDAR alignment of one million kilometers at a continent scale, as a foundation for autonomous driving safety analysis

Janusz Bedkowski [1,†,‡], Hubert Nowak [2,†,‡], Blazej Kubiak [3,†,‡], Witold Studzinski [4,†,‡], Maciej Janeczek [5,†,‡], Szymon Karas [6,†,‡], Adam Kopaczewski [7,†,‡], Przemyslaw Makosiej [8,†,‡], Jaroslaw Koszuk [9,†,‡], Michal Pec [10,†,‡] and Krzysztof Miksa [11,†,‡]

[1] TomTom B.V.; Janusz.Bedkowski@tomtom.com
[2] TomTom B.V.; Hubert.Nowak@tomtom.com
[3] TomTom B.V.; Blazej.Kubiak@tomtom.com
[4] TomTom B.V.; Witold.Studzinski@tomtom.com
[5] TomTom B.V.; Maciej.Janeczek@tomtom.com
[6] TomTom B.V.; Szymon.Karas@tomtom.com
[7] TomTom B.V.; Adam.Kopaczewski@tomtom.com
[8] TomTom B.V.; Przemyslaw.Makosiej@tomtom.com
[9] TomTom B.V.; Jaroslaw.Koszuk@tomtom.com
[10] TomTom B.V.; Michal.Pec@tomtom.com
[11] TomTom B.V.; Krzysztof.Miksa@tomtom.com
† Current address: Stefana Zeromskiego 94C, 90-550 Lodz, Polska
‡ These authors contributed equally to this work.

Abstract: This paper concerns a new methodology for accuracy assessment of global positioning system verified experimentally with LiDAR (Light Detection and Ranging) data alignment at continent scale for autonomous driving safety analysis. Accuracy of GPS (Global Positioning System) positioning of an autonomous driving vehicle within a lane on the road is one of the key safety considerations. Safety is addressed as a geometry of the problem, where the aim is to maintain knowledge that the vehicle (its bounding box) is within its lane. Accuracy of GPS positioning is checked by comparing it with mobile mapping tracks in the recorded high definition source. The aim of the comparison is to see if the GPS positioning remains accurate up to the dimensions of the lane where the vehicle is driving. For this reason, a new methodology is proposed. Methodology is composed of six elements: 1) Mobile mapping system minimal setup, 2) Global positioning data processing, 3) LiDAR data processing, 4) Alignment algorithm, 5) Accuracy assessment confirmation and 6) Autonomous driving safety analysis. The research challenge is to assess positioning accuracy of moving cars taking into account the constraints of the coverage of limited access highways in the United States of America. The available coverage limits the possibility of repeatable measurements and introduces an important challenge being the lack the ground truth data. State-of-the-art methods are not applicable for this particular application, therefore a novel approach is proposed. The method is to align all the available LiDAR car trajectories to confirm the GNSS+INS (Global Navigation Satellite System + Inertial Navigation System) accuracy. For this reason, the use of LiDAR metric measurements for data alignment implemented using SLAM (Simultaneous Localization and Mapping) was investigated, assuring no systematic drift by applying GNSS+INS constraints. SLAM implementation used state-of-the-art observation equations and the Weighted Non-Linear Least Square optimization technique that enables integration of the required constraints. The methodology was verified experimentally using arbitrarily chosen measurement instruments (NovAtel GNSS+INS, LiDAR Velodyne HDL32) mounted onto mobile mapping systems. The accuracy was assessed and confirmed by the alignment of 32785 trajectories with total length of 1,159,956.9 km and of total $186.4 * 10^9$ optimized parameters (six degrees of freedom of poses) that cover the United States region in the 2016–2019 period. It is demonstrated that the alignment improves the trajectories, thus final map is consistent.

The proposed methodology extends the existing methods of global positioning system accuracy assessment focusing on realistic environmental and driving conditions. The impact of global positioning system accuracy on autonomous car safety is discussed. It is shown that 99% of the assessed data satisfies the safety requirements (driving within lanes of 3.6 m) for Mid-Size (width 1.85 m, length 4.87 m) vehicle and 95% for 6-Wheel Pickup (width 2.03–2.43 m, length 5.32–6.76 m). The conclusion is that this methodology has great potential for global positioning accuracy assessment at global scale for autonomous driving applications. LiDAR data alignment is introduced as a novel approach to GNSS+INS accuracy confirmation. Further research is needed to solve the identified challenges.

Keywords: global positioning, SLAM; GNSS+INS; road survey; mobile mapping; autonomous driving safety

1. Introduction

Problem statement: The goal of presented research is to measure the impact of global positioning system on autonomous driving safety. The research challenge is to assess positioning accuracy of moving cars taking into account the constraints of the coverage of limited access highways in the USA. Due to the nature of the measurement it is difficult to perform repeatable data collections since cars never follow the same trajectories. The actual coverage limits the possibility of repetitive measurements and introduces an important challenge being lack of the ground truth data. Therefore, the repeatability test method e.g. [1] is not applicable. Thus, accuracy assessment requires a new approach that is formulated as a novel measurement methodology discussed in this paper.

Problem formulation: Accuracy of GPS (Global Positioning System) positioning of an autonomous driving vehicle within a lane on the road is one of the key safety considerations. Safety is addressed as a geometry of the problem, where the aim is to maintain knowledge that the vehicle (its bounding box) is within its lane. Accuracy of GPS positioning is checked by comparing it with mobile mapping tracks in the recorded high definition source. The aim of the comparison is to see if the GPS positioning remains accurate up to the dimensions of the lane where the vehicle is driving. For this reason, a new methodology is proposed. The problem is to confirm the global positioning system accuracy assessed in our case by state-of-the-art NovAtel algorithm and relate it to autonomous driving safety. The localization accuracy requirements for US freeway operation that are discussed in [2] are addressed. It is investigated how to use LiDAR metric measurements to align all available trajectories to confirm the global positioning accuracy assessed by NovAtel algorithm [3]. This required visiting the same places many times which was assessed using a mobile mapping road survey performed at a continent scale. Based on this data collection many challenges were determined and addressed in the paper. Some of the challenges are the following: large area coverage, the impact of environmental conditions, dynamic changes of road geometry like roadworks. The most important requirement for calculating alignment is to assure no systematic drift of aligned trajectories. Thus, the alignment method should work by means of Least Squares using assessed trajectories as constraints. Another problem is to maintain the shape of aligned trajectories; thus, motion model must constrain all relative consecutive poses. Bearing in mind the requirements for aligned trajectories, the result is optimal, therefore the confirmation of the assessment accuracy of the trajectories can be applied. It can only be achieved by means of massive data processing performed to obtain quantitatively correct results.

Problem assessment: A new methodology is proposed for global positioning system accuracy assessment to analyze the impact on autonomous driving safety. It was verified experimentally using an arbitrarily chosen measurement instruments. Usage of

Preprints (www.preprints.org) | NOT PEER-REVIEWED | Posted: 17 June 2021 doi:10.20944/preprints202106.0462.v1

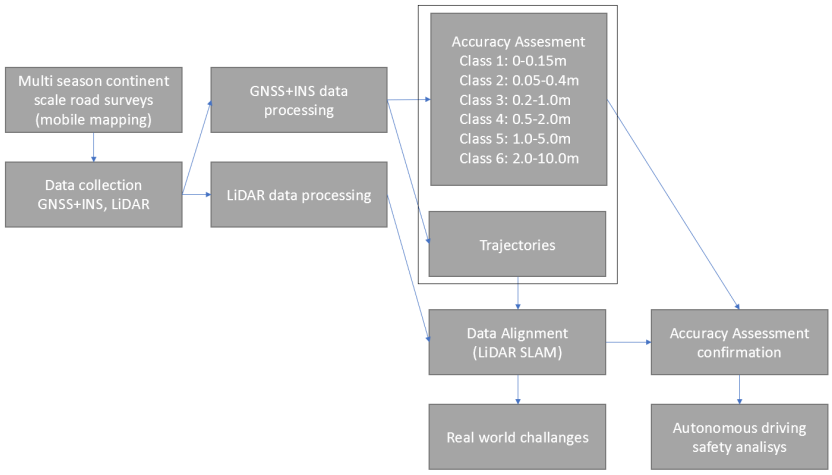

Figure 1. The scheme of the experimental verification of proposed methodology for GNSS+INS accuracy assessment using LiDAR SLAM for autonomous driving safety analysis.

LiDAR metric measurements for alignment as accuracy assessment confirmation tool was investigated. The methodology is composed of six elements:

- Mobile mapping system minimal setup.
- Global positioning data processing.
- LiDAR data processing.
- Alignment algorithm.
- Accuracy assessment confirmation.
- Autonomous driving safety analysis.

The scheme of the experimental verification is shown in Figure 1. To verify the methodology, the accuracy was assessed and confirmed by alignment of 32785 trajectories with total length of 1,159,956.9 km and of total $186.4 * 10^9$ optimized parameters (six degrees of freedom poses) that cover United States region in the 2016–2019 period. The GNSS+INS accuracy of fast-moving vehicles was measured at a large scale, covering as much of the limited access highways in the USA as possible, as realistic dynamic conditions are considered a core requirement. Mobile mapping system architecture, its hardware components, all necessary state-of-the-art observation equations and optimization techniques used for building a SLAM system are explained. The impact of the global positioning system on autonomous driving safety is discussed as it will affect entire society in the near future. GNSS+INS NovAtel was chosen as a reference global positioning measurement instrument mounted on mobile mapping systems equipped with a single Velodyne HDL32 3D LiDAR. GNSS receivers are integrated with mobile mapping systems and the measurements are post-processed using a combination of NovAtel PPP (Precise Point Positioning) and PPK (Post-Processed Kinematic) algorithms, thus obtaining the most accurate positioning from the point of view of applied measurement instrument. This choice of the assessed global positioning system as a reference gives important insights into what can happen when lower quality measurement instruments are used in autonomous cars. To reach satisfactory results it was decided to use mobile mapping data covering most of the limited access highways in the USA. This mobile mapping data consists of GNSS+INS, odometry measurement processed into trajectories (set of consecutive 6DoF poses) and Velodyne HDL32 LiDAR measurements. *The aim of experimental verification of the proposed methodology is to use GNSS+INS trajectories as objects of accuracy assessment, align them using LiDAR data, confirm the accuracy and perform autonomous driving safety analysis.* It is possible only if it is assured that the alignment does not introduce any systematic drift. For this reason the use of the state-of-the-art LiDAR SLAM algorithm was investigated. The algorithm was implemented starting from the beginning using the Weighted Non-Linear Least Square Method capable of

 doi:10.20944/preprints202106.0462.v1

aligning these trajectories based on LiDAR observations, motion model and GNSS + INS constraints. Based on this investigation some deviations in accuracy of GNSS+INS are demonstrated. It is a very important research topic since the era of autonomous driving is approaching. The challenges related to the proposed methodology are addressed. The first challenge is that there is no ground truth for such scope of data. Moreover, accurate tracking of the fleet of fast-moving mobile mapping systems is impossible considering continent scale coverage. The second challenge is assuring no systematic drift in the aligning procedure. The third challenge is related to many factors affecting alignment algorithm relying on LiDAR measurements. The fourth challenge is related to dynamic conditions of the data collection and many environmental changes (e.g. roadworks, weather conditions) that could affect LiDAR-based alignment.

The main requirement is to collect large-scale, mobile mapping data (LiDAR, GNSS+INS) covering as large area as possible and visiting certain locations multiple times. The GNSS+INS accuracy was assessed using LiDAR information. It is advised to use multiple mobile mapping systems with the same setup of the measurement instruments. Thus, the results of the experiments are not affected by bias of using only one measurement instrument. This paper addresses an approach for the continent scale SLAM experiment, which is a contribution to Mobile Robotics domain where the large scale is an interesting research topic. The term "large scale" corresponds to applications where the volume of data and the total length of the trajectories is significant and requires high computational resources to process. For this purpose, the term "continent scale SLAM" is introduced, as it is more adequate for the future autonomous driving systems. This is an important research topic from perspective of recent developments in localization of autonomous cars [4,5]. It is evident that autonomous cars can collect data and contribute to global map updates, thus it is a large-scale problem that inspires many researchers.

The term SLAM [6] corresponds to the "chicken and egg dilemma". Therefore, it is necessary to have a proper map representation that is compatible with observations derived from sensors to localize the vehicle within the map, and accurate localization is needed to build the map. The core concept is the pose that represents position and orientation at a given time. A set of consecutive poses makes up a trajectory. Attaching measurements to the trajectory as relative poses gives an opportunity to reconstruct a map of raw measurements e.g. the point cloud in case of using LiDAR technology. The calibration parameters have to be also considered to assure proper transformation from the trajectory pose to the sensor origin.

This paper concerns the concepts and methods known from Mobile Robotics and Geodesy domains. These domains introduce methodology for map building based on computing absolute pose of measurement instruments assuming raw information typically transformed into feature space [7]. It is addressed how to fill the gap between these domains, which also discussed in [8]. Therefore, the problem of fusing GNSS+INS and LiDAR observations to align all trajectories assuring no systematic drift is the main research topic discussed in this paper. The results of this research is a new methodology of GNSS+INS accuracy assessment. The paper is organized as follows: section 2 discusses the state of the art related to mobile mapping approaches and available data sets. Section 3 concerns an experimental verification of proposed methodology and it defines the minimal setup of mobile mapping systems, GNSS+INS data processing, LiDAR data processing, SLAM algorithm assuring no systematic drift of aligned trajectories and impact on autonomous driving safety. Section 4 addresses real-world challenges affecting data alignment being our important feedback for the research community. In section 5 experimental validation details are provided and the results are discussed in section 5.2. The impact of GNSS+INS positioning on autonomous driving safety is elaborated in section 6. Final conclusions are given in section 7.

2. State of the art

Trajectory, sensor readings and map are terms commonly used in Mobile Robotics in the context of SLAM. Trajectory can be expressed as consecutive 6-DOF poses [9]. Collecting consistent 3D laser data using a moving mobile mapping system is often difficult because the precision of collected data is related to motion estimation. For this reason, trajectory of the sensor during the scan must be taken into account while constructing 3D point clouds. To address this issue many researchers use the stop-scan fashion – they stop a moving platform and take stationary scans [10,11]. On the contrary, in the recent research advances the continuous-time mapping is favored [12,13]. Continuous-time mapping relates to the new term of time calibration method [14], and it introduces a continuous-time, simultaneous localization and a mapping approach for mobile robotics. In comparison, mobile mapping systems used in geodesy use synchronized sensor readings.

Mobile Mapping Systems are composed of proprioceptive, exteroceptive and interoceptive sensors. Proprioceptive sensors measure internal state of the system in the environment such as position, velocity, accelerations, and temperature. Exteroceptive sensors measure parameters external to the system such as pressure, forces and torques, vision, proximity, and active ranging. Vision sensors include monocular, stereo/multiple cameras, equirectangular/spherical cameras, and structured lighting (e.g. so called RGBD cameras). There are active ranging systems laser line scanners, such as: LiDAR, RADAR, and SONAR. Interoceptive sensors measure electrical properties (voltage, current), temperature, battery charge state, stress/strain and sound. All above-mentioned sensors are connected to the dedicated electronics that synchronizes all inputs with GNSS receiver, thus all raw data can be transformed into global reference systems. There is a need to cope with GNSS denied environments, thus recent developments show progress of mobile mapping technologies that also use SLAM algorithms. A mobile mapping device capable of building the map was introduced in [15]. Such devices use the advantage of a rotating LiDAR to perceive full 360-degree distance measurements. Further developments introduce equirectangular cameras that can augment metric information with spherical images. Many mobile mapping applications incorporate equirectangular camera FLiR Ladybug5/5+ to perceive 360-degree spherical images [16]. High-end mobile mapping systems [17] [18] use more precise measurement instruments, which is involves a higher cost.

2.1. Large-scale data sets

In recent research since mobile mapping systems are more and more affordable many open-source large data sets appeared. The GNSS-specific dataset [19] contains GNSS data from two sensors recorded during real-world urban driving scenarios. A mass-market receiver is used, and the ground truth is derived from a highly accurate reference receiver. The complex urban data set [20] provides LiDAR data and stereo images with various position sensors targeting a highly complex urban environment. It captures features in urban environments (e.g. metropolitan areas, complex buildings and residential areas). The data of 2D and 3D of LiDAR is provided. Raw sensor data for vehicle navigation and development tools is given in a ROS file format.

Authors of the Multi Vehicle Stereo Event Dataset [21] provide a collection of data helpful in the development of the 3D perception algorithms for event-based cameras. An interesting data set [22] collects data from the AtlantikSolar UAV (Unmanned Aerial Vehicle) that is a small-sized, hand-launchable, solar-powered device optimized for large-scale aerial mapping and inspection applications. Authors of [23] provide the Oxford RobotCar data set that contains over 100 repetitions of a consistent route through Oxford, United Kingdom, captured over a period of over a year. Additionally, authors provide RTK Ground Truth [24]. Authors of [25] provide the Málaga Stereo and Laser Urban Data Set that was gathered in urban scenarios with a car equipped with stereo camera (Bumblebee2) and five LiDARs. The KITTI-360 data set [26], which is well-

 doi:10.20944/preprints202106.0462.v1

known in Mobile Robotics and Machine Vision domains, collects data from autonomous driving platform called Annieway. For each of the benchmarks, authors also provide an evaluation metrics. They distinguish several use cases: processing raw data [27], performing road benchmark [28], stereo benchmark [29]. Another large-scale dataset: the Kagaru Airborne Stereo data set [30] is a vision dataset gathered from a radio-controlled aircraft flown at Kagaru, Queensland, Australia on 31st August 2010.

2.2. Long-term data sets

Long-term data sets collect multi-season data. The purpose is to address the impact of multi season, varying weather, and other disturbances into localization algorithms. Authors of [31] provide the KAIST multi-spectral data set that covers regions from urban to residential for autonomous systems. They claim that this data set provides different perspectives of the world captured in coarse time slots (day and night) in addition to fine time slots (sunrise, morning, afternoon, sunset, night, and dawn). The interesting Visual-Inertial Canoe data set [32] collects data from a canoe along the Sangamon River in Illinois. Authors claim that the canoe was equipped with a stereo camera, an IMU, and a GPS device, which provide visual data suitable for stereo or monocular applications, inertial measurements, and position data for the ground truth. University of Michigan North Campus Long-Term (NCLT) Vision and LiDAR Dataset [33] consist of omnidirectional (equirectangular) imagery, 3D LiDAR, planar LiDAR, GPS, and proprioceptive sensors for odometry collected using a Segway robot. Authors conducted this research to facilitate researchers focusing on long-term autonomous operation in changing environments. Alderley, Queensland Day/Night Dataset [34] consists of vehicle data for vision-based place recognition with manually annotated ground truth frame correspondences. It is reported that the data set was captured in two different conditions for the same route: one on a sunny day and one during a rainy night.

Outdoor scenario is impacted by change of the environmental conditions and it is related to long-term localization [35] and long-term navigation [36]. The term indoor-outdoor transition [37] sometimes referred to as indoor-outdoor switching corresponds to the scenarios when UV (Unmanned Vehicle) changes location between indoor-like to outdoor-like environments. Indoor environments have a rich set of challenges related to e.g. long-narrow paths, surfaces with limited texture information, thus localization algorithms are affected by perceptual aliasing confusion [38]. The evaluation of the navigation and localization capabilities is performed via the quantitative evaluation of the quality of an estimated trajectory [39].

Lyft [40] - Level 5 Perception Dataset 2020 is relevant as both a large-scale and long-term dataset. It is maintained by the autonomous vehicles that collect raw sensor data on other cars, pedestrians, traffic lights, and more. This dataset features raw LiDAR and camera inputs collected by the autonomous fleet within a bounded geographic area.

2.3. Large scale surveying and mapping

Large scale surveying and mapping relates to the shape of the Earth and spatial relations between objects near its surface. Thus, it is evident that global and local coordinate systems are useful for calculations. To describe position in global reference system (global geocentric Terrestrial system) the coordinates are defined with respect to center of Earth. Spatial relations between objects can be described using a local reference system. 3D Cartesian geocentric coordinates are not very convenient for describing positions on the surface of the Earth. It is actually more convenient to project the curved surface of the Earth on a flat plane, which is related to map projections. Usually, local coordinate system has the y-axis pointing in the North direction, the z-axis in the up direction, and the x-axis completing the pair and therefore pointing in the East direction. This type of system is referred to as topocentric coordinate system. For the coordinates it is common to use the capital letters ENU instead of x, y, z [41] and it is called Local Tangent Plane Coordinates. The alternative way of expressing z coordinate as positive

Preprints (www.preprints.org) | NOT PEER-REVIEWED | Posted: 17 June 2021 doi:10.20944/preprints202106.0462.v1

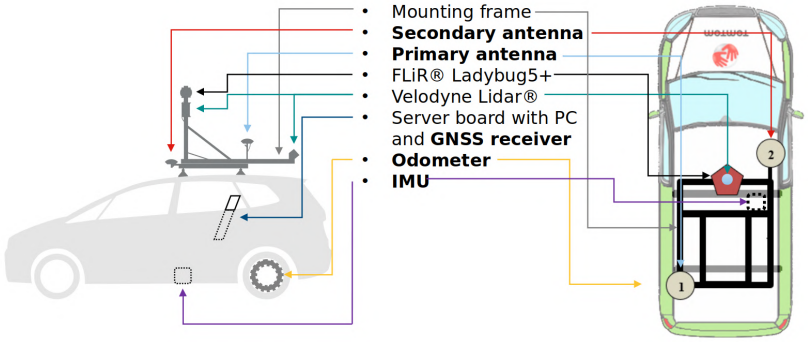

(a)

Figure 2. MoMa van a TomTom B.V. Mobile Mapping proprietary technology providing calibrated data.

number (convenient for airplanes) is NED. All observation equations described in this paper are expressed in right-handed local 3D Cartesian coordinate system, therefore it is important to keep in mind the transformation function from local to global coordinate system looking at the GPS data used for georeferencing [42].

Rigid transformation in **SE**(3) can be separated into two parts: translation and rigid rotation. There are plenty ways to express rotations [43,44] such as using Tait-Bryan and Euler angles, Quaternions [45], Rodriguez [46–48] and e.g. Cayley formula [49]. Further information on how to construct transformation matrices can be found in [50–52]. The information on how to compute derivatives for rotations can be found in [53,54].

3. Experimental verification of the methodology

Experimental verification of the proposed methodology is composed of six elements:

- Mobile mapping system minimal setup (section 3.1) provides necessary information to build the mobile measurement instrument capable of collecting required data sets.
- GNSS+INS data processing (section 3.2) provides information concerning initial trajectories calculation based on NovAtel PPP (Precise Point Positioning) and PPK (Post-Processed Kinematic) algorithms.
- LiDAR data processing (section 3.3) discusses the LiDAR data filtering and classification into basic primitives.
- Alignment algorithm (section 3.4) concerns observation equations and constraints used for building SLAM optimization system.
- GNSS+INS accuracy assessment (section 3.5) explains the accuracy calculations performed using GNSS+INS NovAtel algorithm and confirmed with SLAM alignment.
- Impact on autonomous driving safety (section 3.6).

This methodology enables continent scale GNSS+INS accuracy assessment using massive LiDAR data and SLAM-based trajectory alignment.

3.1. Mobile mapping system minimal setup

The minimal setup of the mobile mapping system is at least one 3D LiDAR, GNSS+INS positioning system and odometry. To assess positioning systems other than GNSS+INS an additional measurement instrument should be integrated with mobile mapping data acquisition pipeline. All data should be synchronized. An example of such mobile mapping system is MoMa (Mobile Mapping) van - TomTom B.V. proprietary technology is shown in Figure 2. It is composed of NovAtel ProPak6®/PwrPak7 GNSS receiver, NovAtel VEXXIS GNSS-850 GNSS antennas, ADIS 16488/KVH 1750 Inertial Measurement Unit, DIY odometer, Velodyne Lidar HDL-32E and FLiR Ladybug 5/5+ LD5P. All data is synchronized, and the relative poses of all sensors are obtained from in-house calibration procedure.

Preprints (www.preprints.org) | NOT PEER-REVIEWED | Posted: 17 June 2021 doi:10.20944/preprints202106.0462.v1

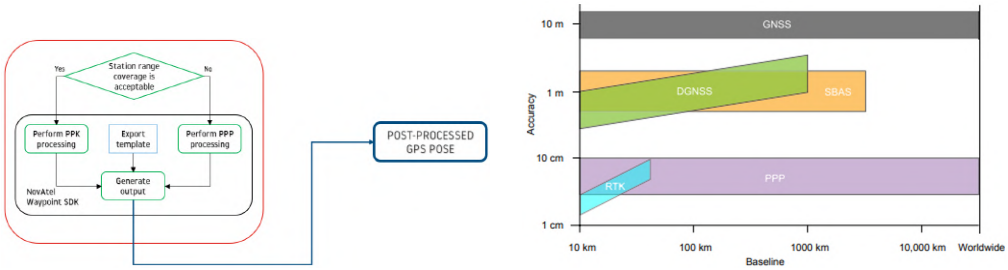

Figure 3. Diagram from "Precise Positioning with NovAtel CORRECT Including Performance Analysis released in 2015 by NovAtel Inc."

Table 1: Quality categories by NovAtel.

NovAtel quality	3D accuracy (m)
1	0.0 - 0.15
2	0.05 - 0.4
3	0.2 - 1.0
4	0.5 - 2.0
5	1.0 - 5.0
6	2.0 - 10.0

3.2. GNSS+INS data processing

GNSS+INS measurements are post-processed using a combination of NovaTel PPP (Precise Point Positioning) and PPK (Post-Processed Kinematic) algorithms shown in Figure 3 - left. All data is processed by NovaTel Waypoint Post-Processing Software SDK (Software Development Kit) 8.90 [3]. PPK and PPP methods incorporate information from GLONASS Satellite Constellation, Satellite Constellation, Geostationary Satellite (GEO) and Reference Stations [55]. The expected accuracy is shown in Figure 3 - right. Due to fact that PPK relates to RTK (Real-Time Kinematic) this method can reach much higher precision compared to PPP. NovAtel introduces 6 classes of accuracy, as shown in Table 1. For the experiment purpose all post-processed GNSS+INS data was transformed to ITRF2008 epoch 2019.0000.

3.3. LiDAR data processing

3D data derived from Velodyne HDL-32 utilizes 32 LiDAR channels aligned from +10.67 to -30.67 degrees to provide an unmatched vertical field of view and a real-time 360-degree horizontal field of view. It generates a point cloud of up to 695,000 points per second with a range of up to 100 m and a typical accuracy of ±2 cm. Reflectivity is used (values 0-255) and 3D coordinates of the measured points in Euclidean space as (x,y,z). In this particular application 3D data is downsampled for equal 3D points distribution and filtered for traffic noise reduction. The remaining point cloud is distinguished into basic primitives (point, cylindrical, plane) and assigned semantic labels related to reflectivity. Therefore, the result is a set of (points with high reflectivity), (points with low reflectivity), (lines with high reflectivity), (lines with low reflectivity), (planes with high reflectivity), (planes with low reflectivity). This segmentation allows matching similar primitives as corresponding landmarks. To distinguish primitives of high and low reflectivity empirically estimated threshold is used, thus 3D points with reflectivity more than 40 are considered as highly reflective and others as having low reflectivity. Traffic noise is a challenging aspect since most of the road surveys were performed in realistic conditions, thus RANSAC (Random Sample Consensus) [56] was applied for extracting surface planes. This method efficiently identifies surface planes even for a large volume of noisy traffic data (Figure 4 - left) and the relevant implementation is available in PCL (Point Cloud Library) [57]. When data is downsampled and filtered, grouping of points into basic primitives as lines, cylinders and planes is

Preprints (www.preprints.org) | NOT PEER-REVIEWED | Posted: 17 June 2021 doi:10.20944/preprints202106.0462.v1

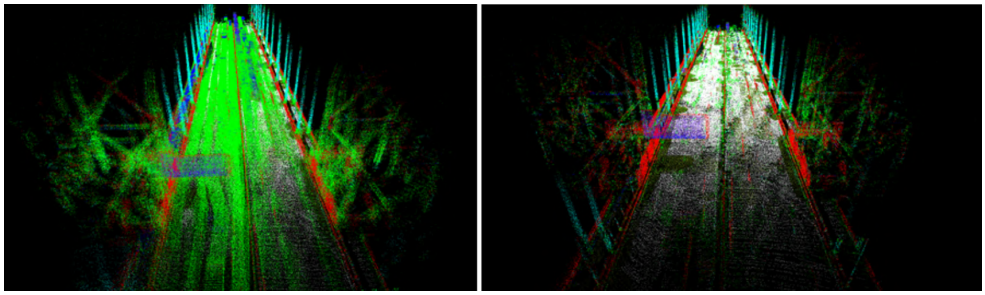

Figure 4. Left - point cloud affected by noise from traffic, right - filtered and classified LiDAR data.

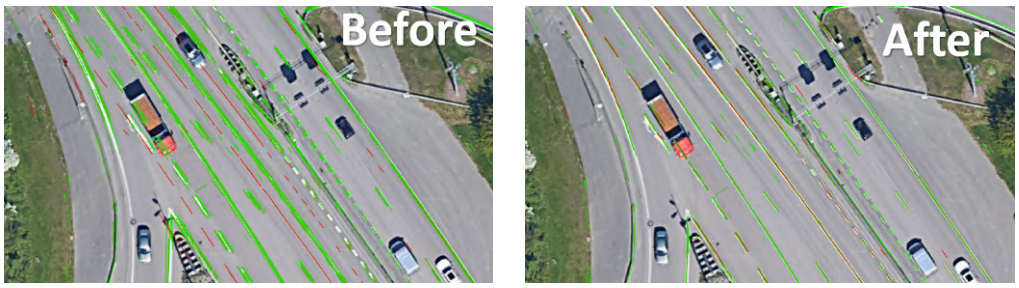

(a) GNSS+INS and processed LiDAR data. **(b)** Aligned data.

Figure 5. Visualization of the alignment algorithm: 1) LiDAR observations have to converge, 2) no systematic drift, 3) aligned trajectories must retain shape. Green - accurate data, red - inaccurate data.

introduced, assuming low-high reflective threshold (Figure 4: right). The result of this classification is the semantic label l assigned for each query point. In that sense the impact of perceptual aliasing confusion [38] is addressed, thus the issue related to outlier observations (incorrectly matched landmarks) is addressed. In literature there are many techniques for automatic classification of point clouds such as semantic Classification of 3D Point Clouds with Multiscale Spherical Neighborhoods [58] that uses local features for classification. Another interesting technique - contour detection in unstructured 3D point clouds was elaborated in [59]. In our application an additional basic primitive as the direction of the line and the normal vector of the plane are calculated and used for constructing observation equations. For calculating the direction of the line and the normal vector of the plane the following covariance matrix is used:

$$\mathbf{C}(N_R) = \frac{1}{N} \sum_{p \in N} (p - \bar{p})(p - \bar{p})^T \tag{1}$$

its eigen-values $\lambda_1 \geqslant \lambda_2 \geqslant \lambda_3 \in \mathbb{R}$ and corresponding eigenvectors $\mathbf{e}_1, \mathbf{e}_2, \mathbf{e}_3 \in \mathbb{R}^3$. where N is the number of points p found in certain radius R and $\bar{p}$ is the centroid of the neighborhood N_R (all points inside the sphere of radius=R). The eigen-values and eigen-vectors are used for local shape description (linearity: equation 2, planarity - equation 3) similar as in [60].

$$Linearity = (\lambda_1 - \lambda_2)/\lambda_1 \tag{2}$$

$$Planarity = (\lambda_2 - \lambda_3)/\lambda_1 \tag{3}$$

The implementation details are available in the form of point cloud processing tutorial available in [61].

3.4. Alignment algorithm

The goal is to find an optimal solution for the desired poses of all GNSS+INS trajectories acquired with MoMa vans assuming information from LiDAR (Figure 5).

Preprints (www.preprints.org) | NOT PEER-REVIEWED | Posted: 17 June 2021 doi:10.20944/preprints202106.0462.v1

The problem is formulated using the Weighted Non-Linear Least Square method, a special case of Generalized Least Squares, known e.g. in photogrammetry [62] and LiDAR data matching [63]. SLAM problem is nonlinear [7] due to rotations, therefore a first-order Taylor expansion is used to construct the design matrix **A**. More information concerning observations and the Least Square method can be found in [64,65]. It is assumed that observational errors are uncorrelated, thus the weight matrix **P** is diagonal and the problem becomes

$$\left(\mathbf{A}^T\mathbf{P}\mathbf{A}\right)\Delta\mathbf{x} = \mathbf{A}^T\mathbf{P}\mathbf{b} \tag{4}$$

Larger values of elements in **P** determine higher impact of the observation equation on optimization process. Similar approach can be found in work on continuous 3D scan matching [13] where authors additionally incorporated a Cauchy function applied to the residuals **b** to cope with outliers. To solve a single iteration as

$$\Delta\mathbf{x} = \left(\mathbf{A}^T\mathbf{P}\mathbf{A}\right)^{-1}\left(\mathbf{A}^T\mathbf{P}\mathbf{b}\right) \tag{5}$$

the sparse Cholesky factorization [66] is used. More implementation details concerning semantic data registration are available as Lesson 16 of tutorial [61].

Rotation matrix representation as Tait-Bryan angles [52] is used. Angles associated with the sequence (x, y, z) correspond to (ω,φ,κ) as (roll, pitch, yaw). They are commonly used in aerospace engineering and computer graphics. In the three-dimensional space rotations via each axis are given:

$$\mathbf{R}_x(\omega) = \begin{pmatrix} 1 & 0 & 0 \\ 0 & cos(\omega) & -sin(\omega) \\ 0 & sin(\omega) & cos(\omega) \end{pmatrix}, \mathbf{R}_y(\varphi) = \begin{pmatrix} cos(\varphi) & 0 & sin(\varphi) \\ 0 & 1 & 0 \\ -sin(\varphi) & 0 & cos(\varphi) \end{pmatrix}, \mathbf{R}_z(\kappa) = \begin{pmatrix} cos(\kappa) & -sin(\kappa) & 0 \\ sin(\kappa) & cos(\kappa) & 0 \\ 0 & 0 & 1 \end{pmatrix} \tag{6}$$

Therefore, rotation matrix **R** is expressed as:

$$\mathbf{R}_{\omega\varphi\kappa} = \begin{pmatrix} cos(\varphi)cos(\kappa) & -cos(\varphi)sin(\kappa) & sin(\varphi) \\ cos(\omega)sin(\kappa)+sin(\omega)sin(\varphi)cos(\kappa) & cos(\omega)cos(\kappa)-sin(\omega)sin(\varphi)sin(\kappa) & -sin(\omega)cos(\varphi) \\ sin(\omega)sin(\kappa)-cos(\omega)sin(\varphi)cos(\kappa) & sin(\omega)cos(\kappa)+cos(\omega)sin(\varphi)sin(\kappa) & cos(\omega)cos(\varphi) \end{pmatrix} \tag{7}$$

and finally the optimization problem concerns finding updates $\Delta\mathbf{x}_{ij}$ for all trajectory poses composed of six parameters including translation part (x,y,z) and rotation part (ω, φ, κ)

$$\Delta\mathbf{x}_{ij} = \left(\Delta x_{ij}, \Delta y_{ij}, \Delta z_{ij}, \Delta\omega_{ij}, \Delta\varphi_{ij}, \Delta\kappa_{ij}\right) \tag{8}$$

where i corresponds to i^{th} trajectory and j corresponds to j^{th} pose.

In the proposed methodology the required observation equations forming SLAM alignment are defined:

- Semantic point-to-point (subsection 3.4.1).
- Semantic point-to-projection (subsection 3.4.2).
- Motion model and GNSS+INS as relative poses constraints (subsection 3.4.3).

Similar approaches can be found in [9,13,67–70] and the implementation of SLAM [71]. It is worth to mention another family of observation equations that corresponds to local geometric features - called surfels in [13]. This particular application of SLAM has to assure no systematic drift of aligned trajectories. For this reason assessed GNSS+INS input trajectories are treated as constraints implemented using relative pose observation equation (subsection 3.4.3). It means that the desired relative pose $\mathbf{P}^t$(x,y,z,ω,φ,κ) between input GNSS+INS trajectory node and aligned one is $\mathbf{P}^t$(0,0,0,0,0,0). Another important aspect of proposed methodology requires no change of the shape of aligned trajectories, thus motion model (as consecutive relative poses of GNSS+INS input trajectories) is used as a constraint also implemented as relative pose observation equation (subsection 3.4.3). In this case the desired relative pose between consecutive nodes of aligned trajectories is calculated from GNSS+INS input trajectories and constrains the

Preprints (www.preprints.org) | NOT PEER-REVIEWED | Posted: 17 June 2021 doi:10.20944/preprints202106.0462.v1

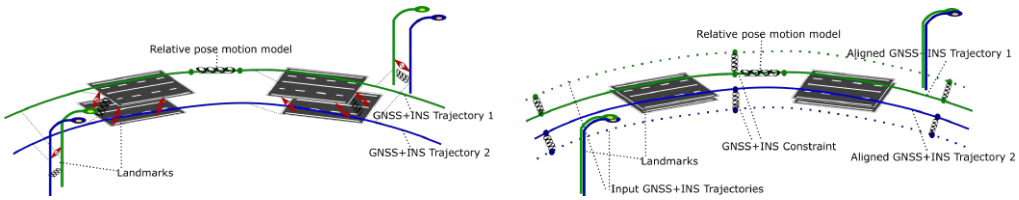

(a) GNSS+INS input trajectories. **(b)** Aligned trajectories.

Figure 6. The idea of aligning trajectories assuring no systematic drift by incorporating GNSS+INS input data as the constraints. Springs visualize the constraints.

optimization process. This approach guarantees similar shape of aligned trajectories to the input data which is crucial for our application. In that sense the optimization process will try to maintain shape, positions and orientations of all input trajectories. All the LiDAR-based observation equations can affect the above-mentioned constraints to minimize the displacement of corresponding landmarks observed from different viewpoints. The idea is presented in Figure 6.

3.4.1. Semantic point-to-point observation equation

The raw LiDAR measurement is represented as source point $P^s(x^s,y^s,z^s)$ in Euclidean space as point in a local reference frame. The matrix [**R**,T] is the transformation of source point P^s into target point $P^t(x^t,y^t,z^t)$ in global reference frame, thus

$$\Psi_{\mathbf{R},T}(x^s,y^s,z^s) = P^t = [\mathbf{R},T]P^s \tag{9}$$

The transformation [**R**,T] has a unique representation as a pose $(x,y,z,\omega,\varphi,\kappa)$, composed of position (x,y,z) and orientation (ω,φ,κ). Orientation corresponds to Tait-Bryan angles respectively $\omega : x-axis, \varphi : y-axis, \kappa : z-axis$ and the x-y-z convention for [**R**,T] building is incorporated. Formula 10 denotes the point-to-point observation equation used in optimization, where there are C pair-correspondences of source point to target point.

$$\min_{\mathbf{R},T} \sum_{i=1}^{C} \left((x_i^t,y_i^t,z_i^t) - \Psi_{\mathbf{R},T}(x_i^s,y_i^s,z_i^s)\right)^2 \tag{10}$$

Semantic point-to-point observation equation is defined by Equation 11, where there are C^l correspondences of neighboring points with the same semantic label l.

$$\min_{\mathbf{R},T} \sum_{i=1}^{C^l} \left((x_{i,l}^t,y_{i,l}^t,z_{i,l}^t) - \Psi_{\mathbf{R},T}(x_{i,l}^s,y_{i,l}^s,z_{i,l}^s)\right)^2 \tag{11}$$

Semantic labels are assigned during LiDAR data processing (section 3.3).

3.4.2. Semantic point-to-projection observation equation

Classification into planes and lines enables incorporating the point-to-projection observation equations. These observations are derived from matching points having the same semantic label. It means that observations are built from points with the same local shape characteristics. It is evident that once these projections are calculated using the above described point-to-point approach they can be used as the observation equations. Look at the projection of point $P^{src,l}(x^{src,l},y^{src,l},z^{src,l})$ that can be transformed to global coordinate system as point $P^{src,g}(x^{src,g},y^{src,g},z^{src,g})$ using matrix [**R**,T]. Thus,

$$\begin{bmatrix} x^{src,g} \\ y^{src,g} \\ z^{src,g} \end{bmatrix} = \Psi_{\mathbf{R},T}(x^{src,l},y^{src,l},z^{src,l}) = [\mathbf{R},T] \begin{bmatrix} x^{src,l} \\ y^{src,l} \\ z^{src,l} \end{bmatrix} \tag{12}$$

Preprints (www.preprints.org) | NOT PEER-REVIEWED | Posted: 17 June 2021 doi:10.20944/preprints202106.0462.v1

to find point $P^{src,g}$ to line projection as $P^{proj,g}$ in global reference system line representation is used as target direction vector $V^{trg,ln}(x^{trg,ln}, y^{trg,ln}, z^{trg,ln})$ and target point on line $P^{trg,g}(x^{trg,g}, y^{trg,g}, z^{trg,g})$ expressed in global reference system. Therefore, the point-to-line projection is as follows:

$$P^{proj,g} = P^{trg,g} + \frac{a \cdot b}{b \cdot b} b, a = \begin{bmatrix} x^{src,g} - x^{trg,g} \\ y^{src,g} - y^{trg,g} \\ z^{src,g} - z^{trg,g} \end{bmatrix}, b = \begin{bmatrix} x^{trg,ln} \\ y^{trg,ln} \\ z^{trg,ln} \end{bmatrix} \tag{13}$$

where $(\cdot)$ is a dot product.

To find point $P^{src,g}$ to plane projection as $P^{proj,g}$ the following plane equation is considered:

$$ax + by + cz + d = 0, \left\| \begin{bmatrix} a & b & c \end{bmatrix} \right\| = 1 \tag{14}$$

$V^{pl} = (a, b, c)$ is the unit vector orthogonal to plane and d is the distance from the origin to the plane. It satisfies following condition with point in 3D space

$$\begin{bmatrix} a & b & c & d \end{bmatrix} \begin{bmatrix} x \\ y \\ z \\ 1 \end{bmatrix} = 0 \tag{15}$$

Therefore projection $P^{proj,g}$ can be computed with:

$$P^{proj,g} = \begin{bmatrix} x^{src,g} \\ y^{src,g} \\ z^{src,g} \end{bmatrix} - \left(\begin{bmatrix} x^{src,g} \\ y^{src,g} \\ z^{src,g} \end{bmatrix} \cdot V^{pl} \right) V^{pl} \tag{16}$$

where $(\cdot)$ is a dot product. To build point-to-line projection or point-to-plane projection observation Equation 11 can be incorporated.

3.4.3. Relative pose observation equation

Relative pose observation equation concerns a relative pose $\mathbf{P}$ (x,y,z,ω,φ,κ) from pose $\mathbf{A}_{from}$ to pose $\mathbf{B}_{to}$ ($\mathbf{P} = \mathbf{A}_{from}^{-1}\mathbf{B}_{to}$) and a desired pose $\mathbf{P}^t$, therefore optimization will converge by moving poses $\mathbf{A}_{from}$ and $\mathbf{B}_{to}$ to reach the desired relative pose $\mathbf{P}^t$. To construct observation equation the function $m2v$ is incorporated to compute vector (x,y,z,ω,φ,κ) from matrix $\mathbf{P}$ assuming Tait-Bryan angle convention. Therefore, optimization problem is defined in Equation 17, where (x_i^t,y_i^t,z_i^t,ω_i^t,φ_i^t,κ_i^t) is a target relative pose (the desired one) that the optimization is supposed to converge with.

$$\min_{\mathbf{R}^A, T^A, \mathbf{R}^B, T^B} \sum_{i=1}^{C} \left((x_i^t, y_i^t, z_i^t, \omega_i^t, \varphi_i^t, \kappa_i^t) - m2v(\mathbf{A}_{from}^{-1}\mathbf{B}_{to})_i \right)^2 \tag{17}$$

3.5. GNSS+INS accuracy assessment

Figure 1 shows the implementation of the proposed methodology for GNSS+INS accuracy assessment using LiDAR SLAM data alignment as confirmation tool. Once mobile mapping data covering expected region is collected, it is processed using methods described in section 3.2 and section 3.3. GNSS+INS data processing provides trajectories and accuracy assessment for each node of trajectory as one of the following classes (Class 1: 0–0.15 m, Class 2: 0.05–0.4 m, Class 3: 0.2–1.0 m, Class 4: 0.5–2.0 m, Class 5: 1.0–5.0 m, Class 6: 2.0–10.0 m). To confirm this accuracy assessment LiDAR SLAM alignment is performed for all of these trajectories. This method provides an optimal solution guaranteeing no systematic drift by minimizing distance between landmarks in aligned trajectories. Relative poses are calculated for all corresponding nodes between the input trajectories and the aligned ones. This relative poses are concatenated into histograms

Preprints (www.preprints.org) | NOT PEER-REVIEWED | Posted: 17 June 2021 doi:10.20944/preprints202106.0462.v1

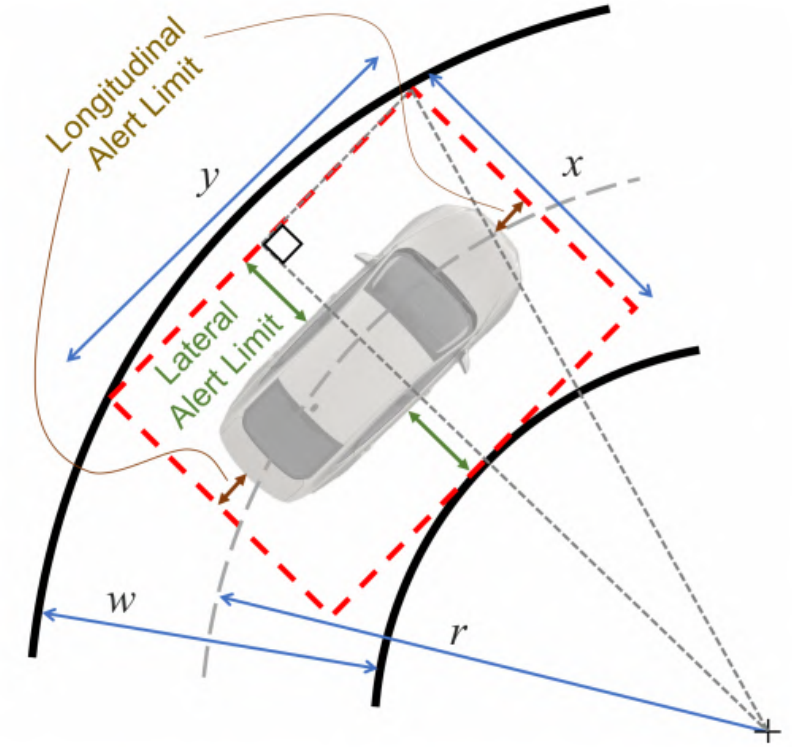

Figure 7. Bounding box geometry duirng a turn maneuver. This shows the allowable maximum position error of the vehicle to ensure it is within the lane known as the alert limits (Figure from [2]).

in section 5.2, therefore it is possible to quantitatively verify the percentage of the data set satisfying certain accuracy condition defined as Class 1–6. It was experimentally proven that accuracy assessment provided by NovAtel GNSS+INS processing tool is very similar to the SLAM output. This confirmed accuracy assessment can be used for considering the impact GNSS+INS positioning on safety discussed in section 6. The cause of SLAM errors is discussed as a real-world challenge in section 4. Due to volume of processed data and manual verification SLAM errors are considered to have minor impact for the overall confirmation of the accuracy assessment.

3.6. Impact on autonomous driving safety

Localization accuracy requirements for US freeway operation that are discussed in [2] are addressed. Safety is addressed as an alert limit for the defined geometry of the problem, where the aim is to maintain knowledge that the vehicle (its bounding box) is within its lane. Horizontally, this is expressed as lateral (side-to-side) and longitudinal (forward-backward) components. Vertically, the vehicle must know what road level it is on (location among multi-level roads). The relationship between the road width and curvature and the bounding box around the vehicle is shown in Figure 7. The relationship between the lateral x and longitudinal y bounds and road geometry w is defined in Equation 18.

$$x = \sqrt{\left(r + \frac{w}{2}\right)^2 - \left(\frac{y}{2}\right)^2} + \frac{w}{2} - r \tag{18}$$

Authors of [2] define alert limits related to the vehicle length l_v and width w_v as 19:

$$\begin{aligned} \textit{Lateral Alert Limit} &= \tfrac{x - w_v}{2} \\ \textit{Longitudinal Alert Limit} &= \tfrac{y - l_v}{2} \end{aligned} \tag{19}$$

Preprints (www.preprints.org) | NOT PEER-REVIEWED | Posted: 17 June 2021 doi:10.20944/preprints202106.0462.v1

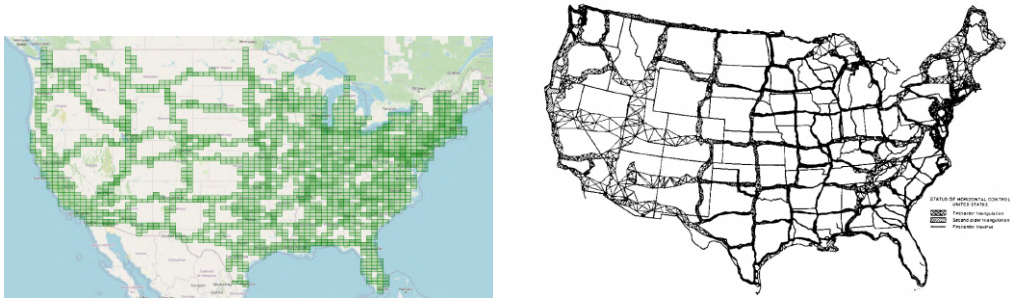

(a) Data collected by TomTom B.V. MoMa cars that were evaluated in this paper.

(b) The triangle net used for creating NAD 27 [8].

Figure 8. Real-world challenge: high volume of data covering United States. Green rectangles correspond to visited regions by MoMa cars collecting data.

For the impact of GNSS positioning on safety the following aspects are considered: vehicle type, a mean distance between lanes of 3.6 m (limited access highways in the United States of America), Lateral Alert Limit and Longitudinal Alert Limit. Reference values of accuracy and alert limits of relative positioning for different types of vehicle versus map are shown in Table 2 [2]. It is to be assumed that during an autonomous

Table 2: Localization requirements for US freeway operation with interchanges. This assumes minimum lane widths of 3.6 meters and allowable speeds up to 137 km/h (85 mph).

Vehicle Type	Accuracy (95%)				Alert Limit				Prob. of Failure (Integrity)
	Lateral [m]	Long. [m]	Vertical [m]	Attitude* [deg]	Lateral [m]	Long. [m]	Vertical [m]	Attitude* [deg]	
Mid-Size	0.24	0.48	0.44	0.51	0.72	1.40	1.30	1.50	10^{-9} / mile (10^{-8} / hour)
Full-Size	0.23	0.48	0.44	0.51	0.66	1.40	1.30	1.50	10^{-9} / mile (10^{-8} / hour)
Standard Pickup	0.21	0.48	0.44	0.51	0.62	1.40	1.30	1.50	10^{-9} / mile (10^{-8} / hour)
Passenger Vehicle Limits	0.20	0.48	0.44	0.51	0.57	1.40	1.30	1.50	10^{-9} / mile (10^{-8} / hour)
6-Wheel Pickup	0.14	0.48	0.44	0.51	0.40	1.40	1.30	1.50	10^{-9} / mile (10^{-8} / hour)

*Error in each direction (roll, pitch, and heading).

drive the same GNSS+INS system is used for positioning and the real-time calculations have the same accuracy as in postprocessing presented in the experiment. It is expected that alert limits will be satisfied throughout the trip, so that the car is safely positioned within lanes. Alert limits should be satisfied for all vehicle types assessed in [2] driving on limited access highways in the United States of America (mean distance between lanes is 3.6 m) and when all assessed GNS+INS data are Class 1 and Class 2 (positioning accuracy 0–0.4 m). In other cases, the assessed global positioning accuracy exceeds alert limit violations and the percentage of such data is the result of measuring the impact on safety.

4. Real-world challenges

To reconstruct the map of a continent e.g. North America it is necessary to cope with many challenges caused by the volume of data (Figure 8) and errors related to raw data acquired in different times. For the comparison the original triangle net used in geodesy [8] is also shown. The dominant issue is related to the gap between two time-intervals where data was acquired, thus changes in the observed environment could occur having negative impact on SLAM convergence and finally the result could yield a suboptimal solution.

Preprints (www.preprints.org) | NOT PEER-REVIEWED | Posted: 17 June 2021 doi:10.20944/preprints202106.0462.v1

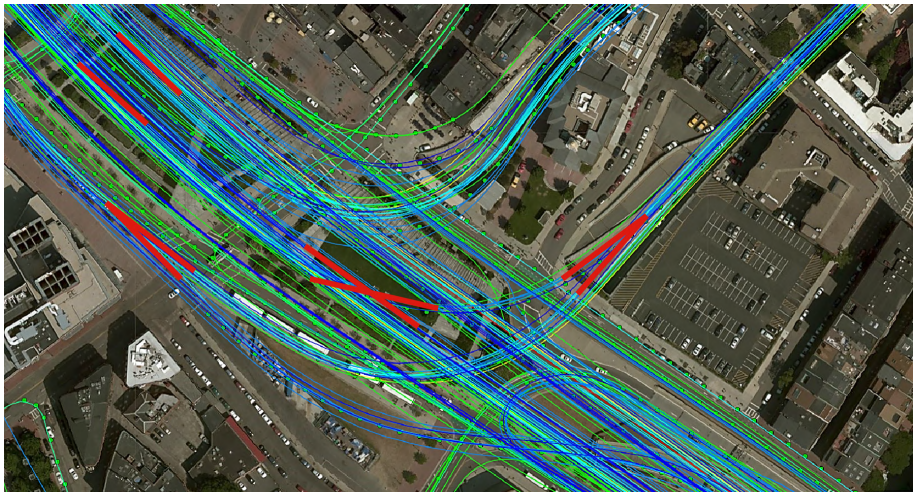

Figure 9. Real-world challenge: high volume of data because of the need of full coverage of the environment - the city sector covered by many trajectories of MoMa vans.

Another challenge is related to having a sufficient coverage of the map, thus it is evident that many places have to be observed (visited) many times to reduce the possible impact of factors such as noisy data, low quality data, heavy traffic (Figure 4), etc. The area is covered sufficiently when there are many overlaps from LiDAR measurements point of view. As in many mobile mapping approaches it is advised to guarantee at least 70% coverage (70% of LiDAR data from one trajectory can find correspondences to LiDAR data of other trajectories). Figure 9 demonstrates a multi-session SLAM subsystem covering city subarea. This region had to be visited many times (colored lines) since the scene is composed of multilevel constructions such as overpassing roads and underground tunnels. Red lines show challenging multi-session correspondences such as multilevel underground cross section etc. SLAM techniques require as good correspondences between observations as possible, thus any disruptive information can affect the algorithm convergence making it a suboptimal solution. After the experiment it was found that in some cases it was almost impossible to automatically find the correspondences between sessions where geometrical or other changes appeared. Therefore, the observed real-world challenges were classified into certain classes: a) lack of observations (Figures 10,11), b) roadworks (Figure 12), c) vegetation (Figure 13), d) repainting (Figure 14), e) multi level changes 15, f) unknown obstacles (Figure 16). Such classification is proposed due to different impact on alignment process. In the current form of the SLAM implementation these challenges are addressed by motion model and GNSS+INS constraints that maintain the poses of the trajectories. The most challenging problem is repainting of the lane dividers since a rather small discrepancy between the old and new paintings can affect alignment. Fortunately, this issue does not affect the entire accuracy assessment, since a large volume of data is processed and the probability of repainting all lane dividers in the whole United States region is rather low. Unknown obstacles are considered as point-to-point observation equations.

5. Experimental validation

5.1. Scope of data set

The scope of data covered by the experiment includes 32785 trajectories collected in the USA by MoMa vans between 2016 and 2019. The total length of trajectories is 1,159,956.9 km and 11,526,543 nodes were used in the analysis. Since calculations performed by SLAM take 200 times more 6DOF nodes, the result of optimizing $186.4 * 10^9$ parameters is reported. In Table 3 there is information collected about the distribution of the data source from the point of view of reported NovAtel accuracy. It can be observed

Preprints (www.preprints.org) | NOT PEER-REVIEWED | Posted: 17 June 2021 doi:10.20944/preprints202106.0462.v1

(a) Image view. **(b)** LiDAR view.

(c) Image view. **(d)** LiDAR view.

Figure 10. Real-world challenge: lack of LiDAR observations caused by environmental conditions, (ab) - typical environmental conditions, (cd) - winter conditions, only high reflective surfaces were detected by LiDAR.

Table 3: Quality categories distribution in analyzed data.

NovAtel quality	distance [km]	% of total	3D accuracy (m)
1	710958	61.29	0.0 - 0.15
2	378453	32.63	0.05 - 0.4
3	49335	4.25	0.2 - 1.0
4	14132	1.22	0.5 - 2.0
5	715	0.06	1.0 - 5.0
6	59	0.01	2.0 - 10.0
raw	6304	0.54	-

that most of the accuracies of the input data are within the range of 0.0–1.0 m. Typical scenarios for limited access highways in the USA is shown in Figure 17.

5.2. Results

The major issue within the context of large scale SLAM systems corresponds to availability of the ground truth data. The methodology for evaluating such systems assuming existence of the ground truth data source can be found in [72]. Since the only ground-truth information comes from input GNSS+INS data it can be justified if SLAM moves poses within certain interval. It that sense it is possible to justify how much SLAM had to move trajectories to reach more consistent result. In Table 4 the results are summarized. For each category the difference between GNSS+INS and SLAM result was computed as relative pose. These values were summarized in histograms, therefore it is possible to justify the percentage of data maintaining the reported quality. An interesting observation is that results for the 2D error are more optimistic, therefore it is claimed that the post-processed GNSS+INS data are less precise in altitude what was shown as example in Figure 18. It can be observed in Table 4 that 52.5% of post-processed GNSS+INS data of class 1 are moved not more than 15 cm by SLAM according to the 3D error. 81.7% of data of class 2 are moved not more than 0.4 m by SLAM according to the 3D error. 91.7% of data of class 3 are moved not more than 1.0 m by SLAM according to the 3D error. Looking at the 2D error it is claimed that 84% of data of class 1 are

Preprints (www.preprints.org) | NOT PEER-REVIEWED | Posted: 17 June 2021 doi:10.20944/preprints202106.0462.v1

(a) Image view.

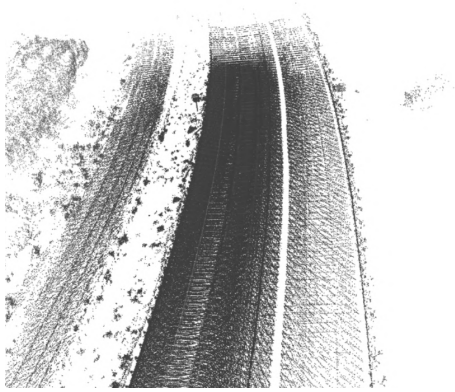

(b) LiDAR view.

(c) Image view.

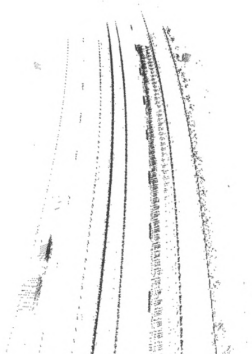

(d) LiDAR view.

Figure 11. Real-world challenge: lack of LiDAR observations caused by environmental conditions, (ab) - typical environmental conditions, (cd) - winter conditions, only high reflective surfaces were detected by LiDAR. It is the same location but MoMa van was driving in opposite directions.

(a) Left - year 2017, right - year 2019.

(b) Left - year 2017, right - year 2018.

(c) Left - year 2017, right - year 2019.

(d) Left - year 2017, right - year 2019.

Figure 12. Real-world challenge - roadworks.

Preprints (www.preprints.org) | NOT PEER-REVIEWED | Posted: 17 June 2021 doi:10.20944/preprints202106.0462.v1

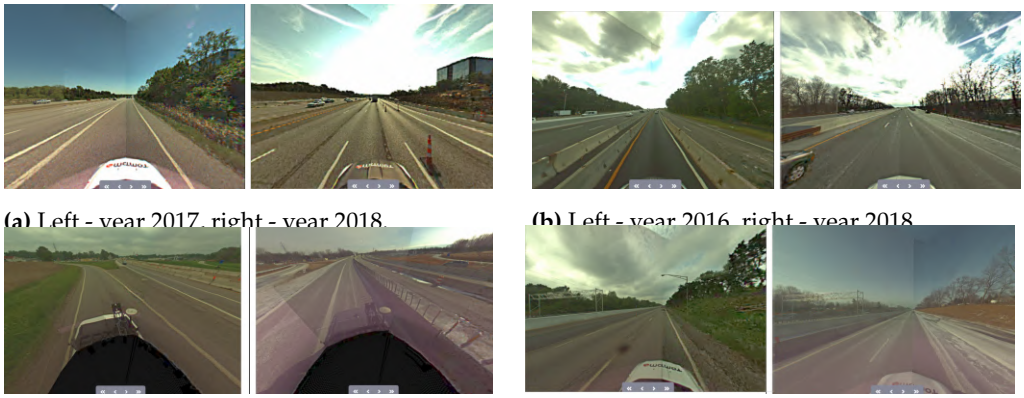

(a) Left - year 2017, right - year 2018. **(b)** Left - year 2016, right - year 2018.

(c) Left - year 2017, right - year 2018. **(d)** Left - year 2017, right - year 2018.

Figure 13. Real-world challenge - vegetation.

(a) Left - year 2018, right - year 2019. **(b)** Left - year 2018, right - year 2018.

(c) Left - year 2018, right - year 2018. **(d)** Left - year 2017, right - year 2019.

Figure 14. Real-world challenge - repainting.

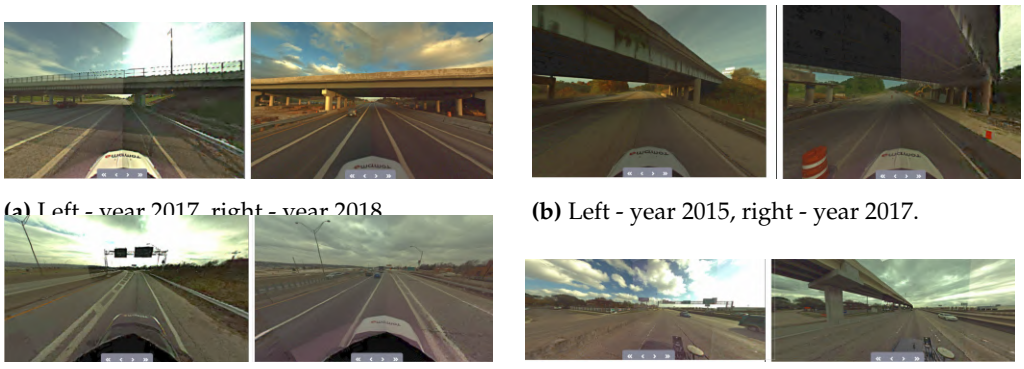

(a) Left - year 2017, right - year 2018. **(b)** Left - year 2015, right - year 2017.

(c) Left - year 2015, right - year 2019. **(d)** Left - year 2015, right - year 2019.

Figure 15. Real-world challenge - multi level changes.

Preprints (www.preprints.org) | NOT PEER-REVIEWED | Posted: 17 June 2021 doi:10.20944/preprints202106.0462.v1

(a) Left - year 2018, right - year 2019.

(b) Left - year 2015, right - year 2019.

(c) Not reflective dots.

(d) Not reflective dots.

Figure 16. Real-world challenge - unknown obstacles and objects of interest. Figure 16a: barriers, Figure 16b: road lateral slope, Figures 16c, 16d: Botts' dots instead of lane dividers.

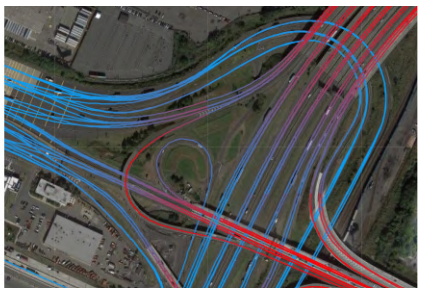

Figure 17. Typical scenarios for limited access highways in the USA.

Preprints (www.preprints.org) | NOT PEER-REVIEWED | Posted: 17 June 2021 doi:10.20944/preprints202106.0462.v1

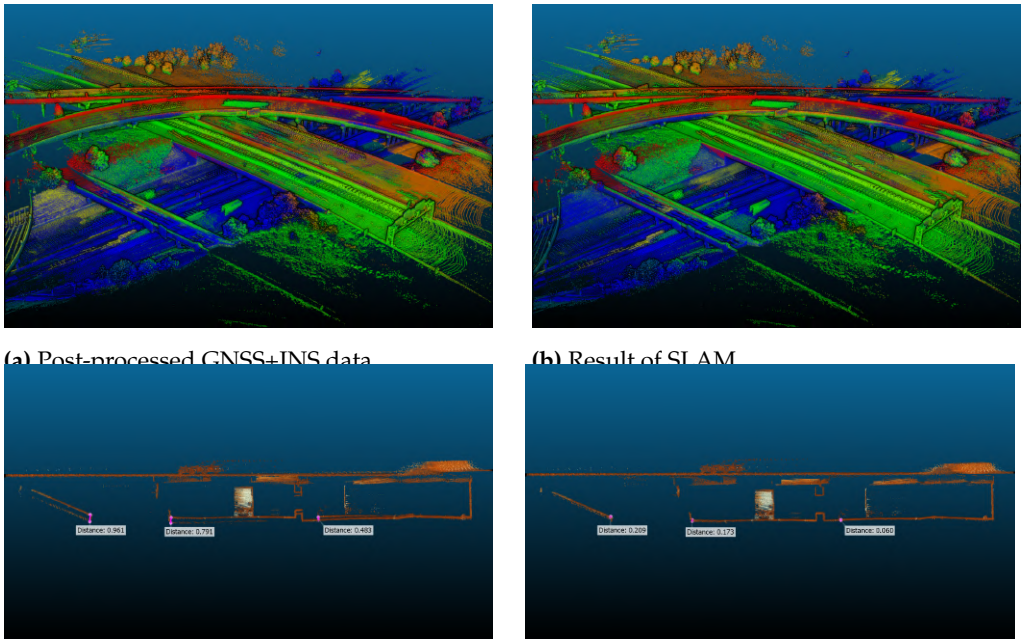

(a) Post-processed GNSS+INS data. **(b)** Result of SLAM.

(c) Post-processed GNSS+INS data. **(d)** Result of SLAM.

Figure 18. The visualization of post-processed GNSS+INS data and SLAM result.

Table 4: Qualities verified using SLAM.

Quality	3D accuracy (m)	% 3D diff	% 2D diff	% Altitude diff
1	0.0 - 0.15	52.5	84.0	65.6
2	0.05 - 0.4	81.7	93.7	88.3
3	0.2 - 1.0	91.7	97.8	94.5
4	0.5 - 2.0	96.1	99.0	97.3
5	1.0 - 5.0	88.6	97.8	91.6
6	2.0 - 10.0	98.4	99.5	99.2

moved by no more than 15 cm by SLAM. Therefore, it can be seen that the accuracy of altitude is much worse than the accuracy of longitude and latitude. This observation must be taken into consideration during navigation on multi-level roads. Additionally, the plots of yaw, pitch, roll errors are shown in Figure 20. The most problematic angle is roll since it corresponds mainly with long straight trajectories where this angle is difficult to measure by IMU, therefore SLAM produces the most significant corrections. An interesting observation is that there are many situations where the accuracy of post-processed GNSS+INS data is better than reported by NovAtel. It can be seen e.g. on Figure 32 where it is evident that large amount of data around 60% has 3D accuracy better than 0.5 m. Manual inspection was performed using HD map of the SLAM alignment and based on the inspection it is concluded that this technique can confirm the accuracy assessed by NovAtel algorithm and it can improve trajectories even when some minor errors of SLAM appear. The causes of these errors were collected as challenges in section 4. The investigation of SLAM errors is going to be the focus of our future research. Figures 19-34 demonstrate the quantitative results collected in Table 4.

6. Impact of GNSS+INS positioning on safety

For the impact of GNSS positioning on safety the following aspects are considered: a hypothetical Mid-Size vehicle type, a mean distance between lanes as 3.6 m (limited access highways in the United States of America) and Lateral Alert Limit as 0.72 m and Longitudinal Alert Limit as 1.40 m according to [2] (as a reference reported values of accuracy and alert limits of relative positioning for different types of vehicle versus

Preprints (www.preprints.org) | NOT PEER-REVIEWED | Posted: 17 June 2021 doi:10.20944/preprints202106.0462.v1

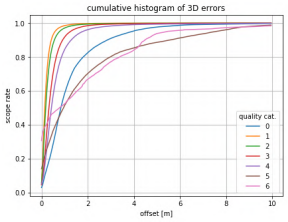

(a) Histograms of the 3D errors.

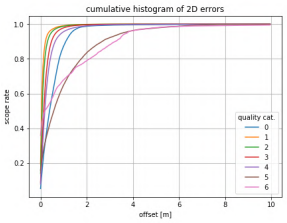

(b) Histograms of 2D errors.

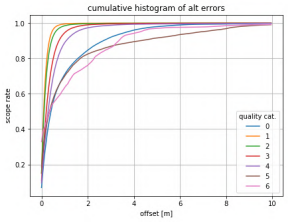

(c) Histograms of altitude errors.

Figure 19. Histograms of 3D, 2D and altitude errors measured as cumulated relative poses between GNSS+INS and SLAM alignment.

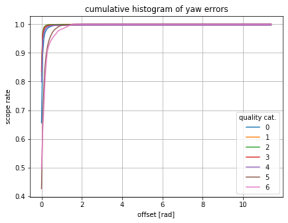

(a) Histograms of yaw errors.

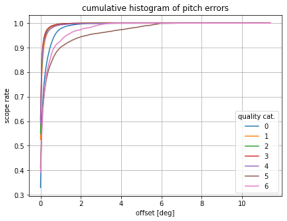

(b) Histograms of pitch errors.

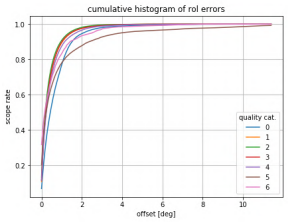

(c) Histograms of roll errors.

Figure 20. Histograms of yaw, pitch, roll errors measured as cumulated relative poses between GNSS+INS and SLAM alignment.

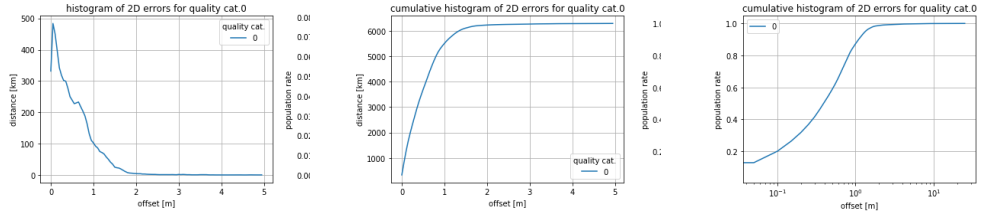

Figure 21. Histograms of 2D errors for category 0 (raw GNSS data) measured as cumulated relative poses between GNSS+INS and SLAM alignment.

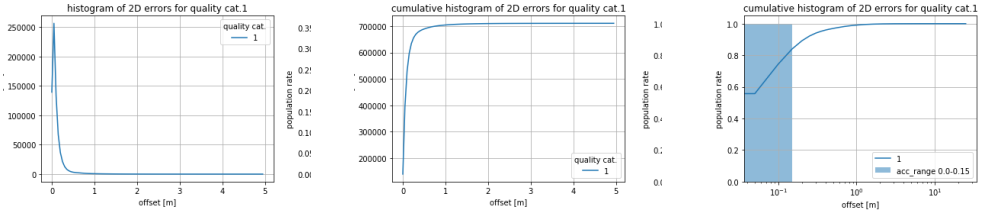

Figure 22. Histograms of 2D errors for data of NovAtel category 1 (accuracy range 0–0.15 m plotted as a blue rectangle) measured as cumulated relative poses between GNSS+INS and SLAM alignment.

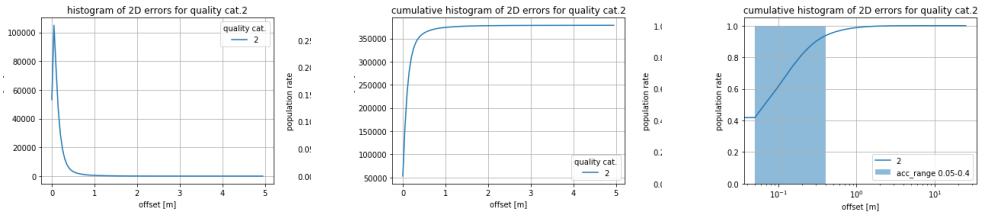

Figure 23. Histograms of 2D errors for data of NovAtel category 2 (accuracy range 0.05–0.4 m plotted as a blue rectangle) measured as cumulated relative poses between GNSS+INS and SLAM alignment.

Preprints (www.preprints.org) | NOT PEER-REVIEWED | Posted: 17 June 2021 doi:10.20944/preprints202106.0462.v1

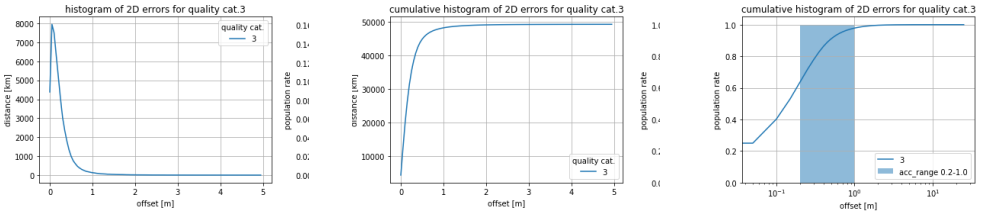

Figure 24. Histograms of 2D errors for data of NovAtel category 3 (accuracy range 0.2–1.0 m plotted as a blue rectangle) measured as cumulated relative poses between GNSS+INS and SLAM alignment.

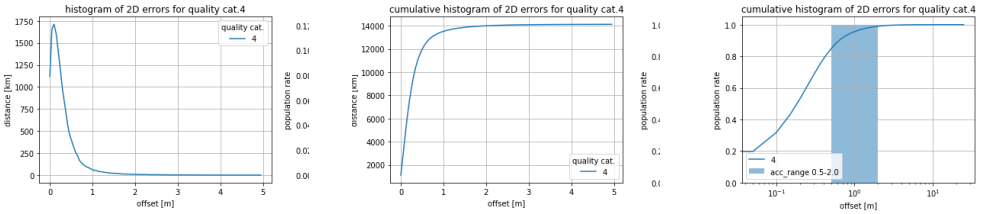

Figure 25. Histograms of 2D errors for data of NovAtel category 4 (accuracy range 0.5–2.0 m plotted as a blue rectangle) measured as cumulated relative poses between GNSS+INS and SLAM alignment.

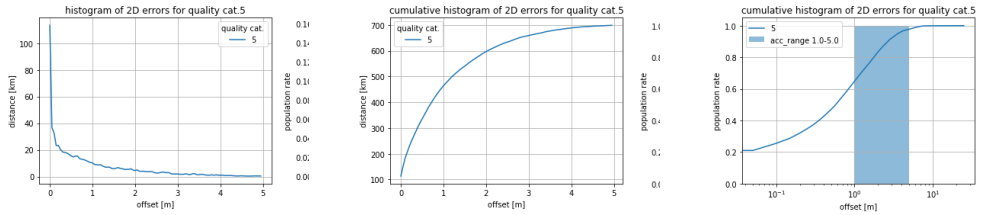

Figure 26. Histograms of 2D errors for data of NovAtel category 5 (accuracy range 1.0–5.0 m plotted as a blue rectangle) measured as cumulated relative poses between GNSS+INS and SLAM alignment.

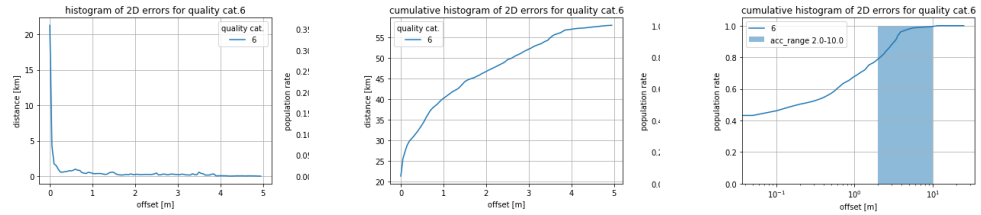

Figure 27. Histograms of 2D errors for data of NovAtel category 6 (accuracy range 2.0–10.0 m plotted as a blue rectangle) measured as cumulated relative poses between GNSS+INS and SLAM alignment.

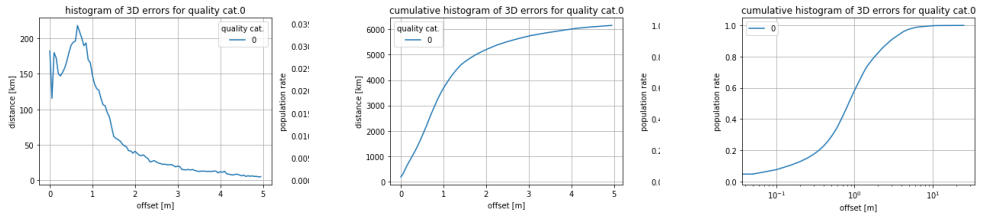

Figure 28. Histograms of the 3D error for category 0 (raw GNSS data) measured as cumulated relative poses between GNSS+INS and SLAM alignment.

Preprints (www.preprints.org) | NOT PEER-REVIEWED | Posted: 17 June 2021 doi:10.20944/preprints202106.0462.v1

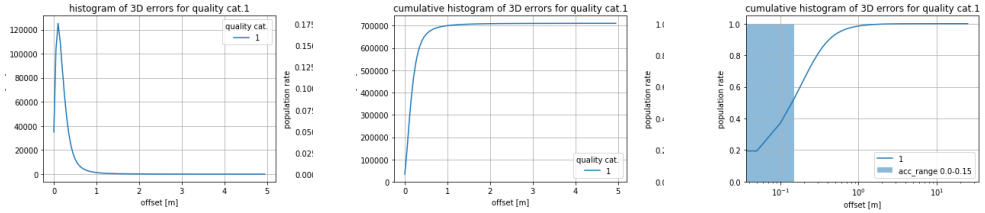

Figure 29. Histograms of the 3D error for data of NovAtel category 1 (accuracy range 0–0.15 m plotted as a blue rectangle) measured as cumulated relative poses between GNSS+INS and SLAM alignment.

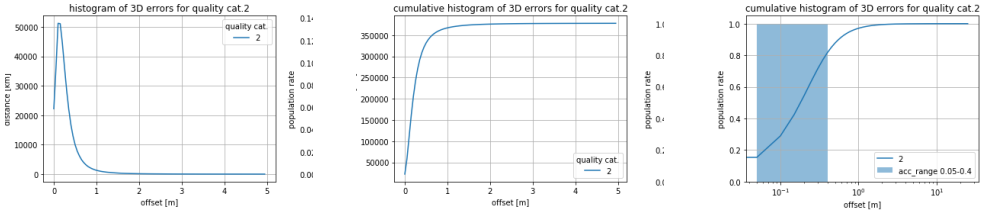

Figure 30. Histograms of the 3D error for data of NovAtel category 2 (accuracy range 0.05–0.4 m plotted as a blue rectangle) measured as cumulated relative poses between GNSS+INS and SLAM alignment.

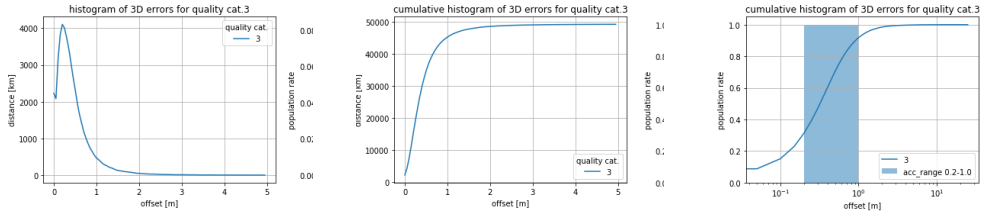

Figure 31. Histograms of the 3D error for data of NovAtel category 3 (accuracy range 0.2–1.0 m plotted as a blue rectangle) measured as cumulated relative poses between GNSS+INS and SLAM alignment.

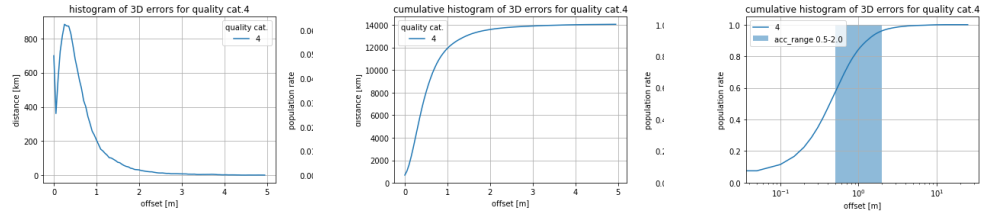

Figure 32. Histograms of the 3D error for data of NovAtel category 4 (accuracy range 0.5–2.0 m plotted as a blue rectangle) measured as cumulated relative poses between GNSS+INS and SLAM alignment.

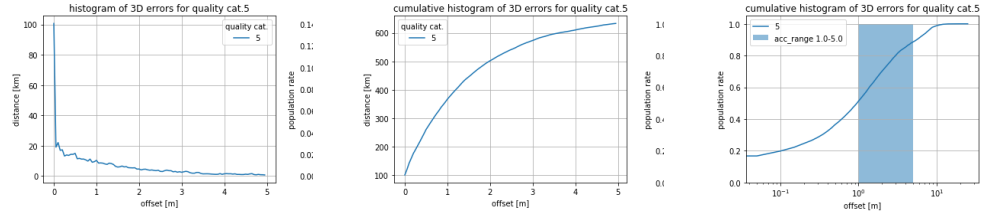

Figure 33. Histograms of the 3D error for data of NovAtel category 5 (accuracy range 1.0–5.0 m plotted as a blue rectangle) measured as cumulated relative poses between GNSS+INS and SLAM alignment.

Preprints (www.preprints.org) | NOT PEER-REVIEWED | Posted: 17 June 2021 doi:10.20944/preprints202106.0462.v1

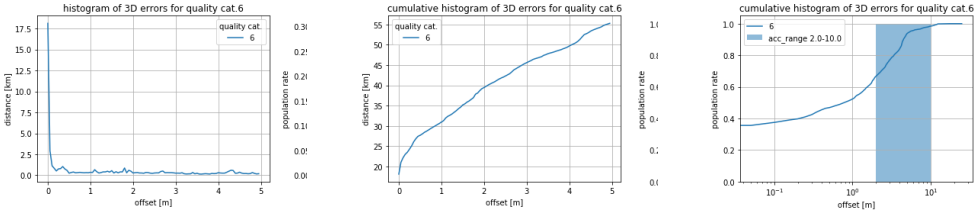

Figure 34. Histograms of the 3D error for data of NovAtel category 6 (accuracy range 2.0–10.0 m plotted as blue rectangle) measured as cumulated relative poses between GNSS+INS and SLAM alignment.

Table 5: 2D error distribution as difference between GNSS+INS trajectories and aligned by LiDAR SLAM.

population [%]	err.below [m]
50	0.0517
68	0.0994
70	0.1083
80	0.1593
90	0.2681
95	0.4267
98	0.7414
99	1.0617
99.7	1.7683
99.99	5.9762

map are shown in Table 2). This scenario is the most optimistic one since a small vehicle is considered. It is assumed that during an autonomous drive there is the same GNSS+INS system for positioning and the real-time calculations have the same accuracy as in postprocessing presented in the experiment. From all trajectories (total length: 1.159.956 km) 710.958 km is class 1 (61.3%), 378.453 is class 2 (32.63%) and 49.335 is class 3 (4.25%). The defined accuracy by NovAtel for class 1 is (0.0 - 0.15 m) for class 2 (0.05–0.4) and class 3 (0.2 - 1.0), thus if the entire data set can reach such classes it can be considered as high probability of satisfying the Alert Limits for Mid-Size (width 1.85 m, length 4.87 m) vehicle localization moving on limited access highways in the United States of America. In our case it is calculated 14.132 km of class 4 (1.22%) 715 km of class 5 (0.006%), 59 km of class 6 (0.005%) and 6304 km of raw data (0.54%). To summarize, 98.17% of processed data belongs to classes 1–3 while 1.83% of data does not belong to classes 1–3 and could cause exceeding the alert limits. To verify these classes, further calculations are peformed related to the alignment of the trajectories as part of the proposed methodology. A result is shown in Table 5 and it is measured as cumulative 2D displacements of the GNSS+INS trajectories to the aligned one. Almost 99% of data satisfies NovAtel 1–3 classes, therefore this additional calculation confirms the fact of more than 1% of data that could cause hitting alert limits for a Mid-Size vehicle. As a further reference altitude error distribution is presented in Table 6 and rotation (roll) error distribution in Table 7. For the larger vehicles e.g. for 6-Wheel Pickup (width 2.03–2.43 m, length 5.32–6.76 m) the Lateral Alert Limit is 0.4 m thus according to the proposed methodology only around 95% of data satisfies it.

6.1. Qualitative example

Consider a route between Los Angeles and San Diego (Figure 35). Figures 36-51 show an interesting subset of identified potential safety issues related to alert limits for this trip. In each figure the left one corresponds to GNSS+INS trajectories (brown color), the right one corresponds to aligned trajectories (also brown color). Lines (LiDAR observations) are marked by blue color. Alerts are marked as red cycles.

Preprints (www.preprints.org) | NOT PEER-REVIEWED | Posted: 17 June 2021 doi:10.20944/preprints202106.0462.v1

Table 6: Altitude error distribution as difference between GNSS+INS trajectories and aligned by LiDAR SLAM.

population [%]	err.below [m]
50	0.1009
68	0.1813
70	0.1919
80	0.2638
90	0.3935
95	0.5441
98	0.8032
99	1.0740
99.7	1.7763
99.99	8.4054

Table 7: Rotation (roll) error distribution as difference between GNSS+INS trajectories and aligned by LiDAR SLAM.

population [%]	err.below [deg]
50	0.2044
60	0.2959
68	0.3939
70	0.4239
80	0.6218
90	1.01
95	1.4414
98	2.0626
99	2.5552
99.7	3.7421
99.99	8.1119

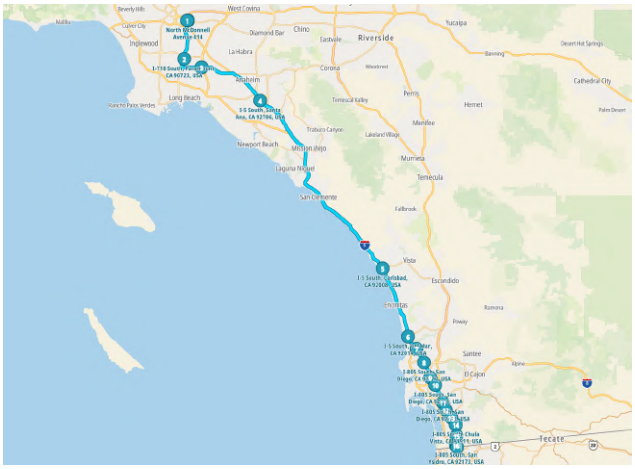

Figure 35. Route between Los Angeles and San Diego with a marked interesting subset of alert limits.

Figure 36. Exceeded alert limit (1) at latitude: 34.0406, longitude: -118.1704

Preprints (www.preprints.org) | NOT PEER-REVIEWED | Posted: 17 June 2021 doi:10.20944/preprints202106.0462.v1

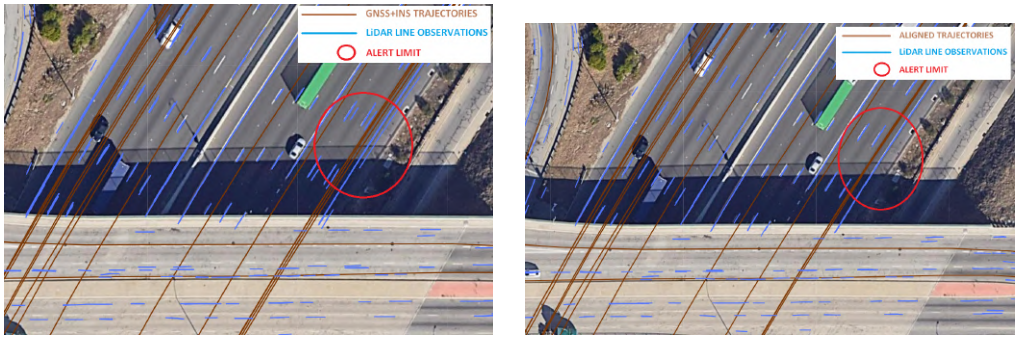

Figure 37. Exceeded alert limit (2) at latitude: 33.9038, longitude: -118.1852

Figure 38. Exceeded alert limit (3) at latitude: 33.8771, longitude: -118.1454

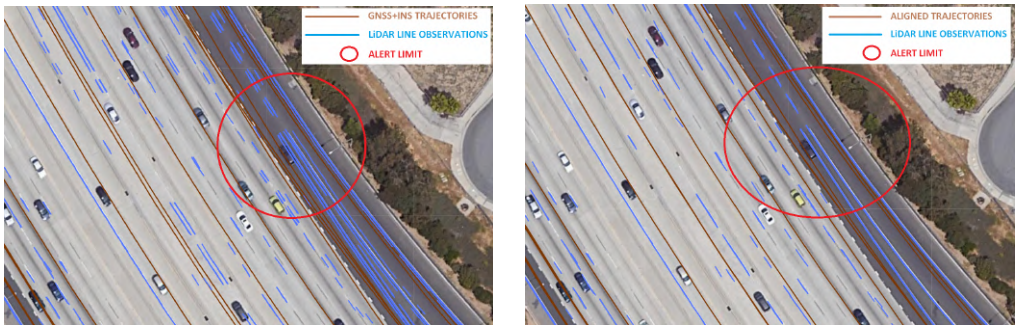

Figure 39. Exceeded alert limit (4) at latitude: 33.7615, longitude: -117.8633

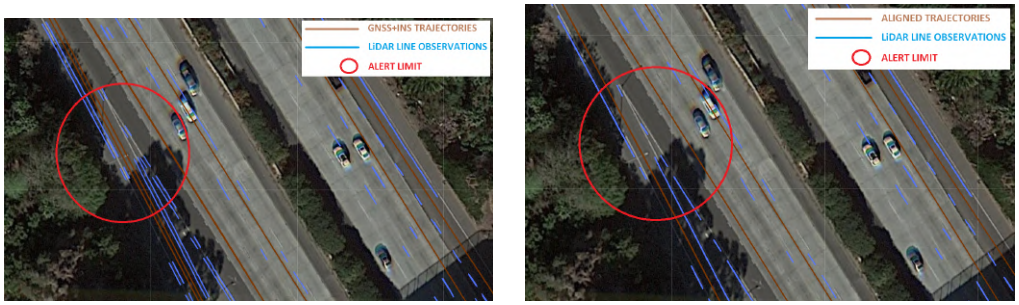

Figure 40. Exceeded alert limit (5) at latitude: 33.1732, longitude: -117.3485

Preprints (www.preprints.org) | NOT PEER-REVIEWED | Posted: 17 June 2021 doi:10.20944/preprints202106.0462.v1

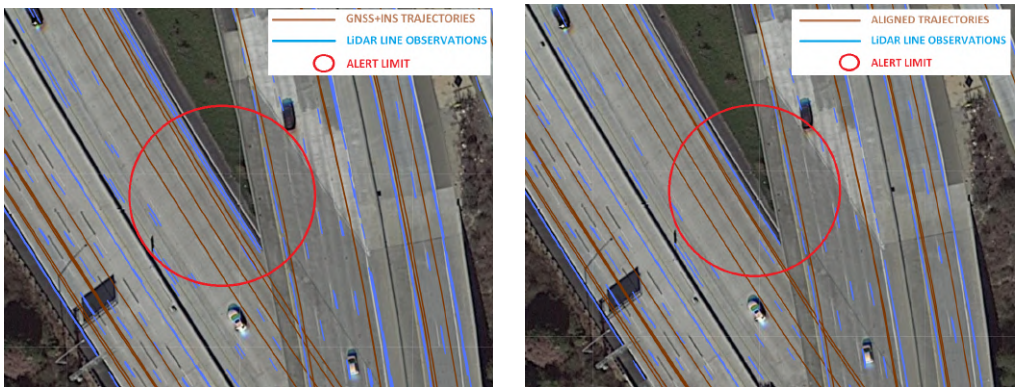

Figure 41. Exceeded alert limit (6) at latitude: 32.9049, longitude: -117.2239

Figure 42. Exceeded alert limit (7) at latitude: 32.8902, longitude: -117.2054

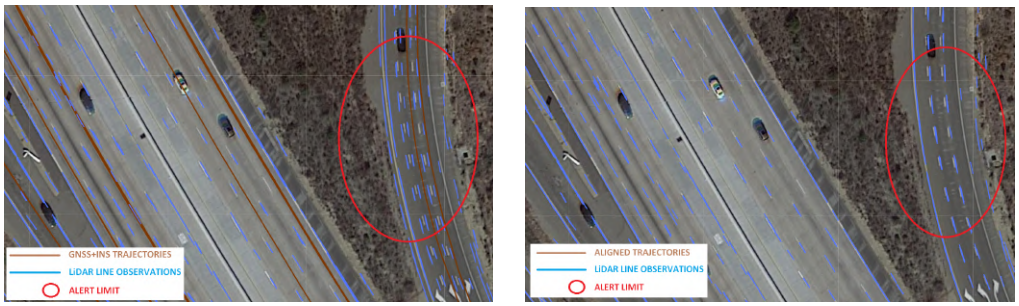

Figure 43. Exceeded alert limit (8) at latitude: 32.8736, longitude: -117.1982

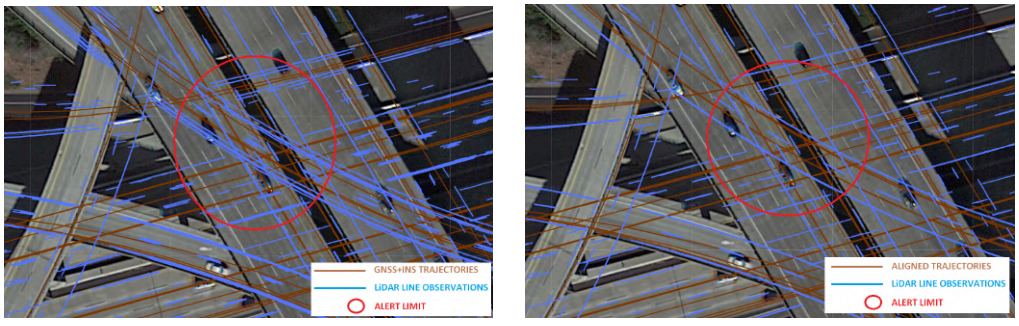

Figure 44. Exceeded alert limit (9) at latitude: 32.7718, longitude: -117.1322

Preprints (www.preprints.org) | NOT PEER-REVIEWED | Posted: 17 June 2021 doi:10.20944/preprints202106.0462.v1

Figure 45. Exceeded alert limit (10) at latitude: 32.7616, longitude: -117.1271

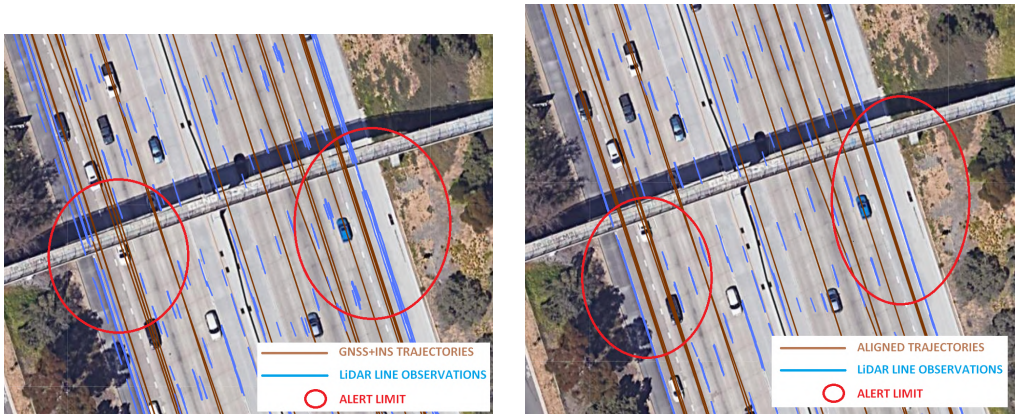

Figure 46. Exceeded alert limit (11) at latitude: 32.6696, longitude: -117.0813

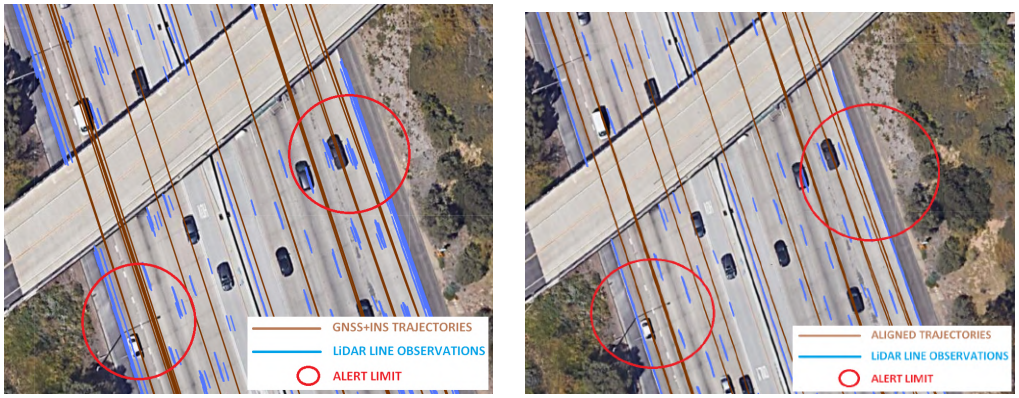

Figure 47. Exceeded alert limit (12) at latitude: 32.6659, longitude: -117.0799

Figure 48. Exceeded alert limit (13) at latitude: 32.6621, longitude: -117.0781

Preprints (www.preprints.org) | NOT PEER-REVIEWED | Posted: 17 June 2021 doi:10.20944/preprints202106.0462.v1

Figure 49. Exceeded alert limit (14) at latitude: 32.6562, longitude: -117.0724

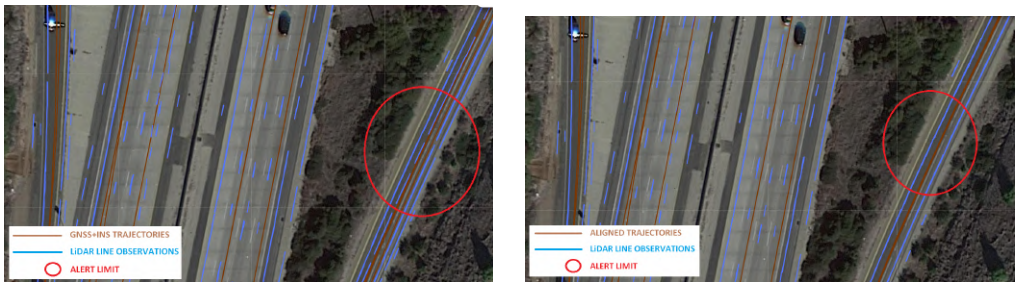

Figure 50. Exceeded alert limit (15) at latitude: 32.5816, longitude: -117.0374

Figure 51. Exceeded alert limit (16) at latitude: 32.5495, longitude: -117.0391

 doi:10.20944/preprints202106.0462.v1

7. Conclusion

This paper concerns a new methodology for accuracy assessment of global positioning system at continent scale for assessing autonomous driving safety. Safety is addressed as an alert limit for the defined geometry of the problem, where the aim is to maintain knowledge that the vehicle (its bounding box) is within its lane. Hypothetical Mid-Size and 6-Wheel Pickup types of vehicles were considered and the mean distance between lanes as 3.6 m as representative boundaries of the vehicles moving on the limited access highways in the United States of America. A new methodology of the global positioning accuracy assessment is proposed, incorporating mapping systems performing road surveys covering United States region in the 2016–2019 period. It is composed of six elements: 1) Mobile mapping system minimal setup, 2) Global positioning data processing, 3) LiDAR data processing, 4) Alignment algorithm, 5) Accuracy assessment confirmation and 6) Autonomous driving safety analysis. It relates to the main goal of measuring the impact of global positioning on autonomous driving safety assessed as calculation of GNSS+INS accuracy confirmed with additional trajectory alignment. The novelty of the approach is the large-scale evaluation based on massive mobile mapping data, GNSS+INS processing for accuracy assessment and introducing LiDAR SLAM-based data alignment to confirm accuracy. The research challenge was to assess the positioning accuracy of the moving cars assuming full coverage of limited access highways in the United States of America. The expected coverage limits the possibility of repetitive measurements and introduces an important challenge of lack of availability of the ground truth data. Therefore, state-of-the-art methodology is not applicable for this particular application and a novel approach is proposed. The idea is to align all trajectories using LiDAR to confirm the accuracy reported by state-of-the-art GNSS+INS data processing performed at a large scale. For this reason, it is investigated how to use of LiDAR metric measurements for data alignment implemented using SLAM (Simultaneous Localization and Mapping) assuring no systematic drift thanks to applying GNSS+INS constraints. The SLAM implementation is using state-of-the-art observation equations and the Weighted Non-Linear Least Square optimization technique capable of integration of required constraints. The methodology was verified experimentally using arbitrarily chosen measurement instruments (NovAtel GNSS+INS, LiDAR Velodyne HDL32) mounted onto mobile mapping systems. The accuracy was assessed and confirmed for 32785 trajectories with total length of 1,159,956.9 km and of total $186.4 * 10^9$ optimized parameters (six degrees of freedom poses) that cover United States region in the 2016–2019 period. The proposed methodology extends the existing methods of global positioning system accuracy assessment with the focus on realistic conditions and full area coverage. The impact of global positioning system accuracy on autonomous car safety is discussed. It is shown that 99% of the assessed data satisfied safety requirements (driving within lanes of 3.6 m) for Mid-Size vehicle and 95% for 6-Wheel Pickup. The conclusion is that this methodology has great potential for global positioning accuracy assessment at global scale for autonomous driving applications. Further research is required to solve challenges affecting data alignment as the reference tool for accuracy confirmation.

Author Contributions: Conceptualization, All; methodology, All; software, All; validation, All; formal analysis, All; investigation, All; resources, All; data curation, All; writing—original draft preparation, J.B; writing—review and editing, All; visualization, All; supervision, K.M; All authors have read and agreed to the published version of the manuscript.

Funding: This research received no external funding.

Data Availability Statement: Not applicable.

Acknowledgments: The authors would like to thank TomTom B.V. for providing access to experimental data, the commercially available product for validation of proposed Methodology and computational resources for performing this experiment.

Conflicts of Interest: The authors declare no conflict of interest.

Abbreviations

The following abbreviations are used in this manuscript:

LiDAR	Light Detection and Ranging
GPS	Global Positioning System
GNSS+INS	Global Navigation Satellite System + Inertial Navigation System
SLAM	Simultaneous Localization and Mapping
RANSAC	Random Sample Consensus

References

1. Lu, D.; Spiegel, D.; Becker, U.; Cai, B.; Wang, J.; Liu, J.; Liu, X. Repeatability test method of GNSS for safe train localisation in real and simulated environments. 2016 IEEE/ION Position, Location and Navigation Symposium (PLANS), 2016, pp. 687–692. doi:10.1109/PLANS.2016.7479762.
2. Reid, T.G.; Houts, S.E.; Cammarata, R.; Mills, G.; Agarwal, S.; Vora, A.; Pandey, G. Localization Requirements for Autonomous Vehicles. *SAE International Journal of Connected and Automated Vehicles* **2019**, *2*. doi:10.4271/12-02-03-0012.
3. NovAtel. https://novatel.com/products/waypoint-post-processing-software, 2021.
4. Im, J.H.; Im, S.H.; Jee, G.I. Extended Line Map-Based Precise Vehicle Localization Using 3D LIDAR. *Sensors* **2018**, *18*.
5. Badue, C.; Guidolini, R.; Carneiro, R.V.; Azevedo, P.; Cardoso, V.B.; Forechi, A.; Jesus, L.; Berriel, R.; Paixão, T.M.; Mutz, F.; de Paula Veronese, L.; Oliveira-Santos, T.; De Souza, A.F. Self-driving cars: A survey. *Expert Systems with Applications* **2021**, *165*, 113816. doi:https://doi.org/10.1016/j.eswa.2020.113816.
6. Leonard, J.; Durrant-Whyte, H. Simultaneous map building and localization for an autonomous mobile robot. *Proceedings IROS '91:IEEE/RSJ International Workshop on Intelligent Robots and Systems '91* **1991**, pp. 1442–1447 vol.3.
7. Skrzypczyński, P. Simultaneous localization and mapping: A feature-based probabilistic approach. *International Journal of Applied Mathematics and Computer Science* **2009**, *19*, 575–588.
8. Agarwal, P.; Burgard, W.; Stachniss, C. Survey of Geodetic Mapping Methods: Geodetic Approaches to Mapping and the Relationship to Graph-Based SLAM. *Robotics and Automation Magazine, IEEE* **2014**, *21*, 63–80. doi:10.1109/MRA.2014.2322282.
9. Bosse, M.; Zlot, R. Continuous 3D scan-matching with a spinning 2D laser. ICRA. IEEE, 2009, pp. 4312–4319.
10. Nuchter, A.; Lingemann, K.; Hertzberg, J.; Surmann, H. 6D SLAM with approximate data association. ICAR '05. Proceedings., 12th International Conference on Advanced Robotics, 2005., 2005, pp. 242–249. doi:10.1109/ICAR.2005.1507419.
11. Silver, D.; Ferguson, D.; Morris, A.; Thayer, S. Topological exploration of subterranean environments. *J. Field Robotics* **2006**, *23*, 395–415. doi:10.1002/rob.20130.
12. Kaul, L.; Zlot, R.; Bosse, M. Continuous-Time Three-Dimensional Mapping for Micro Aerial Vehicles with a Passively Actuated Rotating Laser Scanner. *J. Field Robotics* **2016**, *33*, 103–132. doi:10.1002/rob.21614.
13. Zlot, R.; Bosse, M. Efficient Large-scale Three-dimensional Mobile Mapping for Underground Mines. *J. Field Robotics* **2014**, *31*, 758–779. doi:10.1002/rob.21504.
14. Du, S.; Lauterbach, H.A.; Li, X.; Demisse, G.G.; Borrmann, D.; Nuchter, A. Curvefusion — A Method for Combining Estimated Trajectories with Applications to SLAM and Time-Calibration. *Sensors* **2020**, *20*, 6918.
15. Bosse, M.; Zlot, R.; Flick, P. Zebedee: Design of a Spring-Mounted 3-D Range Sensor with Application to Mobile Mapping. *IEEE Trans. Robotics* **2012**, *28*, 1104–1119.
16. Rau, J.Y.; Su, B.W.; Hsiao, K.W.; Jhan, J.P. SYSTEMATIC CALIBRATION FOR A BACKPACKED SPHERICAL PHOTOGRAMMETRY IMAGING SYSTEM. *The International Archives of the Photogrammetry, Remote Sensing and Spatial Information Sciences* **2016**, *XLI-B1*, 695–702. doi:10.5194/isprs-archives-XLI-B1-695-2016.
17. Toschi, I.; Rodríguez-Gonzálvez, P.; Remondino, F.; Minto, S.; Orlandini, S.; Fuller, A. ACCURACY EVALUATION OF A MOBILE MAPPING SYSTEM WITH ADVANCED STATISTICAL METHODS. *ISPRS - International Archives of the Photogrammetry, Remote Sensing and Spatial Information Sciences* **2015**, *XL-5/W4*, 245–253. doi:10.5194/isprsarchives-XL-5-W4-245-2015.
18. Brede, B.; Lau, A.; Bartholomeus, H.M.; Kooistra, L. Comparing RIEGL RiCOPTER UAV LiDAR Derived Canopy Height and DBH with Terrestrial LiDAR. *Sensors* **2017**, *17*. doi:10.3390/s17102371.
19. Reisdorf, P.; Pfeifer, T.; Breßler, J.; Bauer, S.; Weissig, P.; Lange, S.; Wanielik, G.; Protzel, P. The Problem of Comparable GNSS Results – An Approach for a Uniform Dataset with Low-Cost and Reference Data. The Fifth International Conference on Advances in Vehicular Systems, Technologies and Applications; Ullmann, M.; El-Khatib, K., Eds., 2016, Vol. 5, p. 8. ISSN: 2327-2058.
20. Jeong, J.; Cho, Y.; Shin, Y.S.; Roh, H.; Kim, A. Complex urban dataset with multi-level sensors from highly diverse urban environments. *The International Journal of Robotics Research* **2019**, p. 0278364919843996.
21. Zhu, A.Z.; Thakur, D.; Özaslan, T.; Pfrommer, B.; Kumar, V.; Daniilidis, K. The Multi Vehicle Stereo Event Camera Dataset: An Event Camera Dataset for 3D Perception. *CoRR* **2018**, *abs/1801.10202*, [1801.10202].
22. Oettershagen, P.; Stastny, T.; Mantel, T.; Melzer, A.; Rudin, K.; Gohl, P.; Agamennoni, G.; Alexis, K.; Siegwart, R. Long-Endurance Sensing and Mapping using a Hand-Launchable Solar-Powered UAV. Field and Service Robotics : Results of the 10th

International Conference; Wettergreen, D.S.; Barfoot, T.D., Eds.; Springer: Berlin, 2016; Vol. 113, pp. 441 – 454. 10th International Conference on Field and Service Robotics (FSR 2015); Conference Location: Toronto, Canada; Conference Date: June 24-26, 2015, doi:10.3929/ethz-a-010585180.

23. Maddern, W.; Pascoe, G.; Linegar, C.; Newman, P. 1 Year, 1000km: The Oxford RobotCar Dataset. *The International Journal of Robotics Research (IJRR)* **2017**, *36*, 3–15, [http://ijr.sagepub.com/content/early/2016/11/28/0278364916679498.full.pdf+html]. doi:10.1177/0278364916679498.
24. Maddern, W.; Pascoe, G.; Gadd, M.; Barnes, D.; Yeomans, B.; Newman, P. Real-time Kinematic Ground Truth for the Oxford RobotCar Dataset. *arXiv preprint arXiv: 2002.10152* **2020**.
25. Blanco, J.L.; Moreno, F.A.; Gonzalez-Jimenez, J. The Málaga Urban Dataset: High-rate Stereo and Lidars in a realistic urban scenario. *International Journal of Robotics Research* **2014**, *33*, 207–214. doi:10.1177/0278364913507326.
26. Geiger, A.; Lenz, P.; Urtasun, R. Are we ready for Autonomous Driving? The KITTI Vision Benchmark Suite. Conference on Computer Vision and Pattern Recognition (CVPR), 2012.
27. Geiger, A.; Lenz, P.; Stiller, C.; Urtasun, R. Vision meets Robotics: The KITTI Dataset. *International Journal of Robotics Research (IJRR)* **2013**.
28. Fritsch, J.; Kuehnl, T.; Geiger, A. A New Performance Measure and Evaluation Benchmark for Road Detection Algorithms. International Conference on Intelligent Transportation Systems (ITSC), 2013.
29. Menze, M.; Geiger, A. Object Scene Flow for Autonomous Vehicles. Conference on Computer Vision and Pattern Recognition (CVPR), 2015.
30. Warren, M.; McKinnon, D.; He, H.; Glover, A.; Shiel, M.; Upcroft, B. Large Scale Monocular Vision-only Mapping from a Fixed-Wing sUAS. International Conference on Field and Service Robotics; , 2012.
31. Choi, Y.; Kim, N.; Hwang, S.; Park, K.; Yoon, J.S.; An, K.; Kweon, I.S. KAIST Multi-spectral Day/Night Dataset for Autonomous and Assisted Driving **2018**.
32. Miller, M.; Chung, S.J.; Hutchinson, S. The Visual–Inertial Canoe Dataset. *The International Journal of Robotics Research* **2018**, *37*, 13–20, [https://doi.org/10.1177/0278364917751842]. doi:10.1177/0278364917751842.
33. Carlevaris-Bianco, N.; Ushani, A.K.; Eustice, R.M. University of Michigan North Campus long-term vision and lidar dataset. *International Journal of Robotics Research* **2015**, *35*, 1023–1035.
34. Milford, M.; Scheirer, W.; Vig, E.; Glover, A.; Baumann, O.; Mattingley, J.; Cox, D. Condition-invariant, top-down visual place recognition. 2014 IEEE International Conference on Robotics and Automation (ICRA), 2014, pp. 5571–5577. doi:10.1109/ICRA.2014.6907678.
35. Kim, G.; Park, B.; Kim, A. 1-Day Learning, 1-Year Localization: Long-Term LiDAR Localization Using Scan Context Image. *IEEE Robotics and Automation Letters* **2019**, *4*, 1948–1955. doi:10.1109/LRA.2019.2897340.
36. Churchill, W.; Newman, P. Experience-Based Navigation for Long-Term Localisation. *Int. J. Rob. Res.* **2013**, *32*, 1645–1661. doi:10.1177/0278364913499193.
37. Zhu, Y.; Luo, H.; Wang, Q.; Zhao, F.; Ning, B.; Ke, Q.; Zhang, C. Curvefusion — A Method for Combining Estimated Trajectories with Applications to SLAM and Time-Calibration. *Sensors* **2019**, *4*, 786.
38. Crook, P.A.; Hayes, G. Learning in a State of Confusion: Perceptual Aliasing in Grid World Navigation. IN TOWARDS INTELLIGENT MOBILE ROBOTS 2003 (TIMR 2003), 4 TH BRITISH CONFERENCE ON (MOBILE) ROBOTICS, 2003.
39. Zhang, Z.; Scaramuzza, D. A Tutorial on Quantitative Trajectory Evaluation for Visual(-Inertial) Odometry **2019**. pp. 7244–7251. doi:10.1109/IROS.2018.8593941.
40. Kesten, R.; Usman, M.; Houston, J.; Pandya, T.; Nadhamuni, K.; Ferreira, A.; Yuan, M.; Low, B.; Jain, A.; Ondruska, P.; Omari, S.; Shah, S.; Kulkarni, A.; Kazakova, A.; Tao, C.; Platinsky, L.; Jiang, W.; Shet, V. Lyft Level 5 Perception Dataset 2020. https://level5.lyft.com/dataset/, 2019.
41. Hotine, M., Geodetic Coordinate Systems. In *Differential Geodesy*; Zund, J., Ed.; Springer Berlin Heidelberg: Berlin, Heidelberg, 1991; pp. 65–89.
42. Gerdan, G.P.; Deakin, R.E. Transforming Cartesian Coordinates X, Y, Z to Geographical Coordinates φ, λ, h. *Australian Surveyor* **1999**, *44*, 55–63, [https://doi.org/10.1080/00050351.1999.10558773].
43. Pujol, J. Hamilton, Rodrigues, Gauss, Quaternions, and Rotations: a Historical Reassessment. *Commun. Math. Anal.* **2012**, *13*, 1–14.
44. Grassia, F.S. Practical Parameterization of Rotations Using the Exponential Map. *Journal of Graphics Tools* **1998**, *3*, 29–48.
45. Joldeş, M.; Muller, J.M. Algorithms for manipulating quaternions in floating-point arithmetic. ARITH-2020 - IEEE 27th Symposium on Computer Arithmetic; IEEE: Portland, United States, 2020; Proceedings of ARITH-2020, IEEE 27th Symposium on Computer Arithmetic, pp. 1–8. doi:10.1109/ARITH48897.2020.00016.
46. Dai, J.S. Euler–Rodrigues formula variations, quaternion conjugation and intrinsic connections. *Mechanism and Machine Theory* **2015**, *92*, 144–152. doi:10.1016/j.mechmachtheory.2015.03.004.
47. Liang, K.K. Efficient conversion from rotating matrix to rotation axis and angle by extending Rodrigues' formula, 2018, [arXiv:cs.CG/1810.02999].
48. Terzakis, G.; Lourakis, M.; Ait-Boudaoud, D. Modified Rodrigues Parameters: An Efficient Representation of Orientation in 3D Vision and Graphics. *J. Math. Imaging Vis.* **2018**, *60*, 422–442. doi:10.1007/s10851-017-0765-x.

49. Özkaldı, S.; Gündoğan, H. Cayley Formula, Euler Parameters and Rotations in 3-Dimensional Lorentzian Space. *Advances in Applied Clifford Algebras* **2010**, *20*, 367–377. doi:10.1007/s00006-009-0148-5.
50. Diebel, J. Representing attitude: Euler angles, unit quaternions, and rotation vectors. *Matrix* **2006**, *58*, 1–35.
51. Blanco, J.L. A tutorial on SE(3) transformation parameterizations and on-manifold optimization. Technical report, University of Malaga, 2010.
52. Gao, X.; Zhang, T.; Liu, Y.; Yan, Q. 14 Lectures on Visual SLAM: From Theory to Practice. Technical report, 2017.
53. Gallego, G.; Yezzi, A. A Compact Formula for the Derivative of a 3-D Rotation in Exponential Coordinates. *Journal of Mathematical Imaging and Vision* **2014**, *51*, 378–384. doi:10.1007/s10851-014-0528-x.
54. Solà, J.; Deray, J.; Atchuthan, D. A micro Lie theory for state estimation in robotics, 2020, [arXiv:cs.RO/1812.01537].
55. NovAtel. https://novatel.com/an-introduction-to-gnss/chapter-5-resolving-errors/gnss-data-post-processing, 2021.
56. Fischler, M.A.; Bolles, R.C. Random Sample Consensus: A Paradigm for Model Fitting with Applications to Image Analysis and Automated Cartography. *Commun. ACM* **1981**, *24*, 381–395. doi:10.1145/358669.358692.
57. Rusu, R.B.; Cousins, S. 3D is here: Point Cloud Library (PCL). IEEE International Conference on Robotics and Automation (ICRA); , 2011.
58. Thomas, H.; Deschaud, J.; Marcotegui, B.; Goulette, F.; Gall, Y.L. Semantic Classification of 3D Point Clouds with Multiscale Spherical Neighborhoods. *CoRR* **2018**, *abs/1808.00495*, [1808.00495].
59. Hackel, T.; Wegner, J.D.; Schindler, K. Contour Detection in Unstructured 3D Point Clouds. 2016 IEEE Conference on Computer Vision and Pattern Recognition (CVPR), 2016, pp. 1610–1618. doi:10.1109/CVPR.2016.178.
60. Bosse, M.; Zlot, R. Continuous 3D scan-matching with a spinning 2D laser. 2009 IEEE International Conference on Robotics and Automation, ICRA 2009, Kobe, Japan, May 12-17, 2009. IEEE, 2009, pp. 4312–4319. doi:10.1109/ROBOT.2009.5152851.
61. Bedkowski, J. GPU computing in robotics. https://github.com/JanuszBedkowski/gpu_computing_in_robotics, 2021.
62. Kraus, K.; Harley, I.A.; Kyle, S. *Photogrammetry: Geometry from Images and Laser Scans*; De Gruyter: Berlin, Boston, 18 Oct. 2011. doi:https://doi.org/10.1515/9783110892871.
63. Gruen, A.; Akca, D. Least squares 3D surface and curve matching. *ISPRS Journal of Photogrammetry and Remote Sensing* **2005**, *59*, 151 – 174. Received: 11 July 2004; Revised: 16 February 2005; Accepted: 16 February 2005; Available online: 29 March 2005.., doi:10.1016/j.isprsjprs.2005.02.006.
64. Mikhail, E.M.; Ackermann, F.E., Observations and least squares. In *Observations and least squares*; University Press of America: Washington, D.C., 1982.
65. Aitken, A. On least squares and linear combination of observations **1934**. *55*, 42–48.
66. Higham, N. Cholesky factorization. *Wiley Interdisciplinary Reviews: Computational Statistics* **2009**, *1*, 251–254. doi:10.1002/wics.18.
67. Besl, P.J.; McKay, N.D. A method for registration of 3-D shapes. *IEEE Transactions on Pattern Analysis and Machine Intelligence* **1992**, *14*, 239–256. doi:10.1109/34.121791.
68. Ranade, S.; Yu, X.; Kakkar, S.; Miraldo, P.; Ramalingam, S. Can generalised relative pose estimation solve sparse 3D registration?, 2019, [arXiv:cs.CV/1906.05888].
69. Zhang, J.; Singh, S. LOAM: Lidar Odometry and Mapping in Real-time. Proceedings of Robotics: Science and Systems Conference, 2014.
70. Shan, T.; Englot, B. LeGO-LOAM: Lightweight and Ground-Optimized Lidar Odometry and Mapping on Variable Terrain. 2018 IEEE/RSJ International Conference on Intelligent Robots and Systems (IROS), 2018, pp. 4758–4765. doi:10.1109/IROS.2018.8594299.
71. Kümmerle, R.; Grisetti, G.; Strasdat, H.; Konolige, K.; Burgard, W. G2o: A general framework for graph optimization. 2011 IEEE International Conference on Robotics and Automation, 2011, pp. 3607–3613. doi:10.1109/ICRA.2011.5979949.
72. Sturm, J.; Engelhard, N.; Endres, F.; Burgard, W.; Cremers, D. A benchmark for the evaluation of RGB-D SLAM systems. 2012 IEEE/RSJ International Conference on Intelligent Robots and Systems, 2012, pp. 573–580. doi:10.1109/IROS.2012.6385773.